Universiteit Leiden
The Netherlands

Pt as a possible spin-orbit coupling source for equal-spin triplets

Westerdijk, Maaike

Citation
Westerdijk, M. (2025). *Pt as a possible spin-orbit coupling source for equal-spin triplets*.

Version:	Not Applicable (or Unknown)
License:	License to inclusion and publication of a Bachelor or Master Thesis, 2023
Downloaded from:	https://hdl.handle.net/1887/4280504

Note: To cite this publication please use the final published version (if applicable).

Pt as a possible spin-orbit coupling source for equal-spin triplets

THESIS

submitted in partial fulfillment of the
requirements for the degree of

MASTER OF SCIENCE
in
PHYSICS

Author :	Maaike Westerdijk
Student ID :	2490471
Supervisor :	Prof.dr. J. Aarts
2nd corrector :	Prof.dr.ir. T.H. Oosterkamp

Leiden, The Netherlands, October 13, 2025

Pt as a possible spin-orbit coupling source for equal-spin triplets

Maaike Westerdijk

Huygens-Kamerlingh Onnes Laboratory, Leiden University
P.O. Box 9500, 2300 RA Leiden, The Netherlands

October 13, 2025

Abstract

There is some controversy on the role of spin-orbit coupling (SOC) in the generation of equal-spin triplets, a pairing state that realizes the superconducting long-range proximity in ferromagnets. In recent years, theoretical descriptions have been developed of superconductor/ferromagnet with SOC systems that predict a long-range triplet component (LRTC) due to SOC. The collection of experimental research on the subject, however, currently does not provide an unambiguous answer, and conclusive evidence of the SOC-generated LRTC remains lacking. This work adds to the body of experimental explorations of SOC as a source for equal-spin triplets. Our approach is twofold: we probe the proximity effect in bilayer films of Nb with Pt/Co, Pt, and Co, and we measure the properties of lateral Nb/Pt/Co/Pt/Nb Josephson junctions where the supercurrent is forced through the Co layer by a trench that we cut with focused ion beam milling. In our films, we find a striking difference in the critical temperatures and zero-temperature coherence lengths of the Nb/Pt/Co sample on the one hand and the Nb/Pt and Nb/Co samples on the other hand. Our junction devices all become fully superconducting which would provide direct evidence for the SOC-generated LRTC, if not for a lack of knowledge about the exact structure of the junction that could be either Nb/Pt/Co/Pt/Nb, Nb/Pt/Nb, or a constriction junction, depending on the trench depth. Interestingly, the temperature dependence of the critical current of these devices is anomalous in the case of a short Nb/Pt/Nb or constriction junction, while triplet transport in junctions with half-metallic ferromagnets theoretically has the same relation. Overall, this work does not end the controversy of the SOC-generated LRTC although it adds some unexpected results that may find their origin in the LRTC.

Contents

1 Introduction **7**

2 Long-range proximity and Rashba spin-orbit coupling **11**
2.1 Proximity effect 12
2.1.1 Long-range proximity with spin-mixing layer 14
2.2 Rashba spin-orbit coupling 15
2.2.1 SOC as long-range triplet source 17

3 Proximity effects in Nb, Pt and Co bilayers **21**
3.1 Sample fabrication 21
3.1.1 Electron-beam lithography 22
3.1.2 Thin film deposition 23
3.2 Critical temperatures 24
3.3 Upper critical fields 26

4 Junctions in Nb/Pt/Co devices **31**
4.1 Device fabrication 31
4.1.1 Thickness of evaporated Pt 33
4.1.2 Focused ion beam milling 35
4.2 Critical temperature and field dependence 36
4.3 Is the trench 'deep enough'? 40

5 Conclusions **45**

Acknowledgments **47**

References **49**

Chapter 1

Introduction

Superspintronics is an emerging field at the intersection of superconductivity and spintronics [1], aiming to use the control of spin degrees of freedom in combination with superconducting currents. By integrating these fields of research, superspintronics can minimize dissipation, promising low-power electronic devices [2]. Fundamentally, the field also probes questions about the interplay between magnetism and superconductivity — two competing forms of order that meet at interfaces between superconductors (S) and ferromagnets (F).

Equal-spin triplets are essential for superspintronics. Not only are they necessary if a superconductor is to sustain a spin-polarized current, but equal-spin Cooper pairs also uniquely provide the possibility of long-range superconducting proximity in ferromagnets, a property that is indispensable to superspintronics. For this reason, equal-spin triplets are often referred to as long-range triplets (LRT) or the long-range triplet component (LRTC), in contrast to the $m_s = 0$ triplets with zero spin-projection, which are short-range (SRT). They are most commonly generated by noncollinear ferromagnetic layers at S/F′/F interfaces [3–5] (see Section 2.1.1). Magnetic inhomogeneity also forms the basis for other methods, such as magnetic texture due to geometry [6] and half-metallic ferromagnets (CrO_2, LSMO) with spin-active interfaces [7–9], both methods that we have previously studied and employed in our group.

A number of recent experimental works have suggested a role for intrinsic spin-orbit coupling (SOC) in the generation of equal-spin triplets. Specifically, most of these experiments involved a thin layer of Pt, a heavy metal with high SOC [10], in combination with the ferromagnet Co. In 2018,

Version of October 13, 2025– Created October 13, 2025 - 11:10

Banerjee *et al.* [11] used an asymmetric Pt/Co/Pt trilayer as an 'effective spin-orbit-coupled ferromagnet' proximity-coupled to 24 nm (18 nm) Nb, and observed a 40 mK (90 mK) suppression of the critical temperature (T_c) when applying a 100 mT in-plane field, a suppression that was absent in their Nb/Pt and Nb/Co/Pt samples. The authors argue that this suppression is due to the generation of equal-spin triplets that are able to 'leak' into the Pt/Co/Pt, reducing T_c.

In a ferromagnetic resonance (FMR) spin-pumping experiment, Jeon *et al.* [12] found significantly larger induced spin currents in the superconducting state than in the normal state when adding spin sink layers with large SOC (Pt, Ta, W) to the Nb/$Ni_{80}Fe_{20}$/Nb trilayer, contrary to expectations for spin-singlet superconductivity. Following up this experiment in 2019, they find further enhancement of the induced spin current when a ferromagnetic layer is added to the Pt [13]. Substituting the Pt/Fe spin sink with Pt/Co/Pt has also allowed them to tune the pumping efficiency by changing the magnetization direction of the Co. What is more, from the use of a Cu spacer, a metal with very weak SOC, they find evidence that the Rashba SOC at the interface between Nb and Pt/Co/Pt is crucial to the generation of pure spin supercurrents in their experiment [14].

Mixed results are reported in 2018 and 2019 by Satchell and Birge [10] regarding vertical stacks of Nb/F/Nb and Nb/Pt/F/Pt/N, using a Co/Ru/Co synthetic antiferromagnet as F. They find that the decay length of the supercurrent in the ferromagnet is the same with and without the SOC layer, apart from a residual supercurrent that is measured in junctions with thicker Co and only with the Pt. However, the effect is small, possibly because their transversal junctions with in-plane magnetization are not suitable for the SOC-generated LRTC as currently proposed in theoretical predictions [15, 16] (see Section 2.2). To account for this fact, Satchell, Loloee, and Birge [17] later revisited their vertical junctions but with a $[Co/Ni]_x$/Co weak link that has canted magnetization. Nonetheless, the I_cR_N product measured for the stacks with a Pt interlayer is 50×-1000× smaller than for the more traditional S-F′-F-F′-S stacks (F′=Ni), and compared with samples that use Cu as the interlayer there are no differences that the authors attribute to SOC.

Yet another type of experiment that links Pt to equal-spin triplets was conducted by Flokstra *et al.* [18] and reported on in 2023. With Pt/Nb and Cu/Nb bilayers they investigated the effect of SOC on the local screening current in the bilayers, as measured with low-energy muon spin-rotation

Version of October 13, 2025– Created October 13, 2025 - 11:10

(LE-μSR). They find a lack of Meissner screening in Pt/Nb, indicating an additional paramagnetic contribution, that they attribute to the net spin of the LRTC. Interestingly, these samples contain no ferromagnetic component, nor do these measurements include any type of charge transport. In that sense, the generation of the LRTC in these bilayers would be a pure equilibrium effect.

Most recently, in 2024, Paschoa *et al.* [19] have also claimed a colossal superconducting spin valve effect in a simple Nb/Pt bilayer that they ascribe to SOC-generated equal-spin triplets. In their measurements of the reduction in T_c as function of the angle of the applied external magnetic field ($\Delta T_c(\theta, B)$), they report a 930 mK difference in $\Delta T_c(90°, 1.5\text{T})$ between their Nb/Pt and Nb/Cu samples. However, Robbins *et al.* [20] doubt the conclusion that this difference is due to the SOC properties of Pt and Cu. With their upper critical field (H_{c2}) measurements of N/S/N trilayers (N = Al, Ti, Cu, Pt, Ta, Au) they argue that conventional orbital screening, rather than spin-triplet pairing, is the dominant mechanism in the suppression of superconductivity under an applied magnetic field.

In summary, the different works that propose a SOC-based mechanism for the forming of equal-spin triplets vary greatly in their experimental realizations, but there is not yet consensus on the matter. If the role of SOC in LRTC generation can be established, these different experiments also beg the question if an exchange field is required. According to Jeon *et al.* [13]'s works and the theoretical predictions [15] the exchange field is explicitly necessary, while Flokstra *et al.* [18]'s research implies it might not be.

In this work, we carry out T_c- and H_{c2}-measurements similar to those of Robbins *et al.* [20] on Nb/Pt/Co, Nb/Pt and Nb/Co bilayers to probe the proximity effect. In addition, we fabricate lateral Nb/Pt/Co/Pt/Nb Josephson junction devices that could potentially prove LRTC generation. Therefore this work contributes to a better understanding of the possible role of SOC in the generation of equal-spin triplets which may well result in new progress in the field of superspintronics. Other questions, regarding the necessity of an exchange field for the LRTC, are outside of the scope of this work and would need to be addressed in the future.

The next chapter in this thesis, Chapter 2, will bring the reader up to speed regarding the key concepts in this thesis, including the proximity effect and a theoretical description of equal-spin triplet generation through SOC. Chapter 3 will describe the fabrication of our Nb/Pt/Co bilayers

Version of October 13, 2025– Created October 13, 2025 - 11:10

and their T_c- and H_{c2} measurements, where we find significant differences between the Nb/Pt/Co film on the one hand and the Nb/Pt and Nb/Co films on the other hand. We make our way from simple films to structured devices in Chapter 4 to measure equal-spin triplet transport in lateral Nb/Pt/Co/Pt/Nb junctions. Although our devices become fully superconducting, a crucial issue is the depth of the trench that determines the nature of our junctions. We conclude our findings in Chapter 5.

Chapter 2

Long-range proximity and Rashba spin-orbit coupling

In a superconductor, electrons near the Fermi surface pair up in Cooper pairs, to then form a bosonic condensate. The electrons themselves however, are fermionic and therefore must obey the Pauli exclusion principle: the wavefunction of the paired state must be antisymmetric. This condition is satisfied if the *product* of the spin, momentum, and frequency symmetries is odd [21].

In a conventional (BCS) superconductor, such as Nb, the spin symmetry is *odd* by nature: the Cooper pairs consist of two electrons with opposite spins, which is referred to as the singlet state (Equation (2.1)). These superconductors are also characterized by their momentum-symmetric s-wave order parameter, and thus they are even-frequency in the case of singlet pairing.

While the singlet pairing has zero net spin ($s = 0, m_s = 0$), the more exotic triplet has $s = 1$, and its spin projection m_s, defined w.r.t. the quantization axis for spin, can be either -1, 0 or 1 (Equation (2.2)). The significance of these properties in the context of the superconducting proximity effect and ferromagnetism is reviewed in Section 2.1, where we describe how equal-spin ($m_s = -1, 1$) triplet pairing can be realized in a ferromagnet by the use of a spin-mixing layer. Furthermore, in Section 2.2 we describe Rashba SOC and discuss a theoretical work on how a ferromagnet with SOC can generate equal-spin triplets.

$$|s, m_s\rangle = \quad |0,0\rangle \quad = \quad \frac{1}{\sqrt{2}}(|\uparrow\downarrow\rangle - |\downarrow\uparrow\rangle) \quad \text{(singlet)} \tag{2.1}$$

$$|s, m_s\rangle = \begin{cases} |1,1\rangle & = & |\uparrow\uparrow\rangle \\ |1,0\rangle & = & \frac{1}{\sqrt{2}}(|\uparrow\downarrow\rangle + |\downarrow\uparrow\rangle) \\ |1,-1\rangle & = & |\downarrow\downarrow\rangle \end{cases} \quad \text{(triplet)} \tag{2.2}$$

2.1 Proximity effect

In the context of superconductivity, the proximity effect refers to the 'leakage' of Cooper pairs at the interface between a superconductor (S) and an adjacent material [21]. Figure 2.1 (a) schematically presents the case that the adjacent material is a nonmagnetic normal metal. In this case, the Cooper pair density (the amplitude of the order parameter, $|\Psi|$) is maximum in S and falls off over a length ξ_S near the S/N interface, then in N further decreases over a length ξ_N before finally dropping to zero. The characteristic length scale ξ is the coherence length and it is a material property. The coherence length of a superconductor follows the relation in Equation (2.3),

$$\xi_S \approx \xi(0)\frac{1}{\sqrt{1 - T/T_c}} \tag{2.3}$$

where T is the temperature, T_c is the critical temperature of the superconductor and $\xi(0)$ is the coherence length at $T = 0\,\mathrm{K}$. For bulk Nb, $\xi(0)$ can be 30 nm to 40 nm, but it is typically smaller (few nm to ∼15 nm) for thin films [22, 23].

For the normal metal, the coherence length is given by Equation (2.4).

$$\xi_N = \sqrt{\frac{\hbar D_N}{k_B T}} \tag{2.4}$$

Here $\hbar$ is the reduced Planck constant, D_N denotes the diffusion coefficient of N, and k_B is the Boltzmann constant. Equation (2.4) is valid in the dirty limit, where ξ_N is smaller than the electron mean free path. Apart from ξ_N as given in Equation (2.4), the interface transparency is also a factor in how well the condensate can 'leak' into the normal metal.

Version of October 13, 2025– Created October 13, 2025 - 11:10

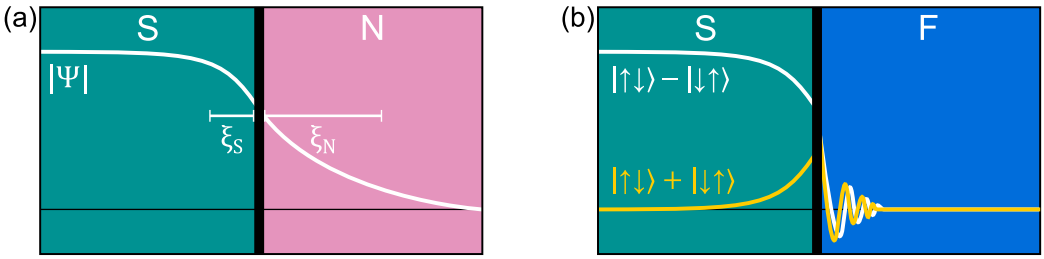

Figure 2.1: *Superconducting proximity effect in:* ***(a)*** *a normal metal N. The magnitude of the order parameter $|\Psi|$ decreases on the S side of the interface over a length ξ_S and leaks into the N side over a length ξ_N.* ***(b)*** *a ferromagnet F. On the S side of the interface the $m_s = 0$ triplet appears. The singlet and $m_s = 0$ triplet oscillate and decay quickly in F.*

We now turn our attention to the case where the adjacent medium is a ferromagnet (F). In contrast to a normal metal, a ferromagnet has an exchange field E_{ex} that shifts the energies of the ↑- and ↓-spin bands by $2E_{ex}$. The exchange field therefore causes an equal but opposite shift in momentum for the spin up and spin down electron of the singlet Cooper pair. A more detailed account of the effect can be found in Ref.[21], but the result is that the momentum shift transforms the singlet state into a linear combination of an oscillating singlet and an oscillating $m_s = 0$ triplet state (with the spin quantization axis defined by the magnetization direction of F), as shown in the F layer in Figure 2.1 (b). The oscillating singlet and $m_s = 0$ triplet can survive in F over a length scale ξ_F (Equation (2.5).

$$\xi_F = \sqrt{\frac{\hbar D_F}{E_{ex}}} \tag{2.5}$$

In strong ferromagnets, such as Co, these correlations fully disappear within only a few nm. For this reason the $m_s = 0$ triplet state is also referred to as the short-range triplet (SRT), in relation to the short-range proximity effect in F.

In addition, there is a spin-dependent interface scattering phase shift [24] that also induces an $m_s = 0$ triplet state on the superconducting side of the interface in Figure 2.1 (b), a mechanism known as *spin-mixing*. Due to the exchange field, the spin-up and spin-down electrons of the singlet Cooper pair have different scattering phase delays $\phi_{\uparrow/\downarrow}$ upon reflection at the S/F interface. The difference between these phase delays defines the spin-mixing angle $\theta = \phi_\uparrow - \phi_\downarrow$ which can be used as a measure of spin-mixing, and the phase shifts are larger for a stronger spin-polarization of

F. A stronger ferromagnet therefore induces more $m_s = 0$ triplets in the superconductor, but they decay more quickly in in the ferromagnet.

2.1.1 Long-range proximity with spin-mixing layer

Long-range proximity *is* possible in ferromagnets if there is magnetic inhomogeneity: if the magnetization direction, and therefore the spin quantization axis, at the interface differs from the magnetization direction in the bulk. This situation can be realized by adding a thin ferromagnetic F′ layer in between the S and F layers.

A sketch of the longe-range proximity mechanism is pictured in Figure 2.2, where we refrain from drawing the oscillating singlet and $m_s = 0$ triplet states in the sketch. If F′ and F have the same magnetization direction, i.e. $M_{F'} \parallel M_F$ (Figure 2.2 (a)), there is no magnetic inhomogeneity and the setup is identical to the S/F interface in Figure 2.1 (b) with only short-range proximity.

In contrast, in Figure 2.2 (b) $M_{F'} \parallel \hat{x}$ while $M_F \parallel \hat{z}$. The $m_s = 0$ triplets that originate from spin-mixing at the S/F′ interface have zero spin-projection *in the $\hat{x}$-direction*, and therefore can decompose into equal-spin triplets ($m_s = -1, 1$) in the $\hat{z}$-direction in the F layer. Evidently, the thickness of the F′ layer is restricted to close to $\xi_{F'}$ (Equation (2.5)) since the $m_s = 0$ triplets must be able to reach the F layer. $M_{F'}$ and M_F can make any non-zero angle to generate the LRT, but a perpendicular orientation such as the one sketched in Figure 2.2 maximizes the equal-spin triplet amplitude.

The length scale over which equal-spin triplets can survive in a ferromag-

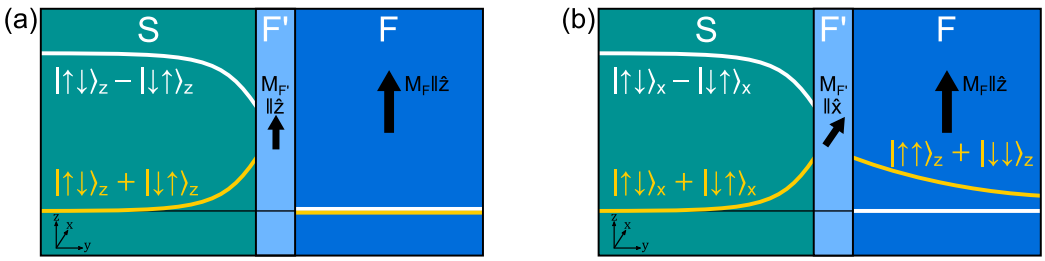

Figure 2.2: *Equal-spin triplet generation.* ***(a)*** *Identical situation to a simple S/F interface where equal-spin triplets are not generated.* ***(b)*** *When the magnetizations of F′ and F make an angle, the long-range triplet is generated at the F′/F interface.*

net is much different from the $m_s = 0$ triplet case, because the exchange field affects both electron spins in the Cooper pair the same. ξ_F^{ES} is therefore dominated by thermal effects, like in the case of singlets in a normal metal, and given by Equation (2.6).

$$\xi_F^{ES} = \sqrt{\frac{\hbar D_F}{k_B T}} \tag{2.6}$$

As a result, the proximity effect of equal-spin triplets in ferromagnets is much more long-range, with a typical decay length of tens of nm in Co [10, 21]. Accordingly, equal-spin triplets are often referred to as long-range triplets (LRT) or long-range triplet component (LRTC).

2.2 Rashba spin-orbit coupling

Spin-orbit coupling (SOC), as a general effect in atomically bound electrons, is a relativistic quantum mechanical effect that constitutes the coupling of an electron's spin angular momentum to its orbital angular momentum. An electron in a bound state orbits the nucleus and therefore moves through a Coulomb field at relativistic speeds. In its rest-frame, the electron experiences the electric field as a magnetic field perpendicular to its momentum [25]. The electron's spin couples to this effective magnetic field, thus the field induces SOC and the momentum-dependent Zeeman energy correction lifts the spin-degeneracy of the energy states (Figure 2.3 (d)). Due to the relativistic nature of the effect, SOC is stronger in materials with high atomic number such as Pt ($Z = 78$) [26, 27].

In systems with spatial inversion asymmetry, such as surfaces and interfaces, there is an additional SOC contribution from the Rashba effect. At an interface for instance, the potential gradient as a result of the two different crystal lattices causes an electric field in the direction of the interface normal. Electrons that move in the plane of the interface therefore experience an in-plane magnetic field perpendicular to their motion, which causes a linear coupling between their spin and their linear momentum [28]. The traditional form of the Rashba correction to the Hamiltonian is expressed in Equation (2.7).

$$H_R = \alpha_R \boldsymbol{\sigma} \cdot (\mathbf{k} \times \hat{\mathbf{n}}) \tag{2.7}$$

Here $\hat{\mathbf{n}}$ denotes the interface normal, $\mathbf{k}$ is the linear momentum and $\boldsymbol{\sigma}$ the spin. The Rashba parameter α_R is a measure of the strength of the cou-

pling. It follows from this term in the Hamiltonian that the Rashba SOC adds a momentum-dependent energy correction $\pm\alpha_R|\mathbf{k}|$ [29] that causes a splitting of the spin energy bands, as illustrated in Figure 2.3 for a free electron in a 2D electron gas (2DEG).

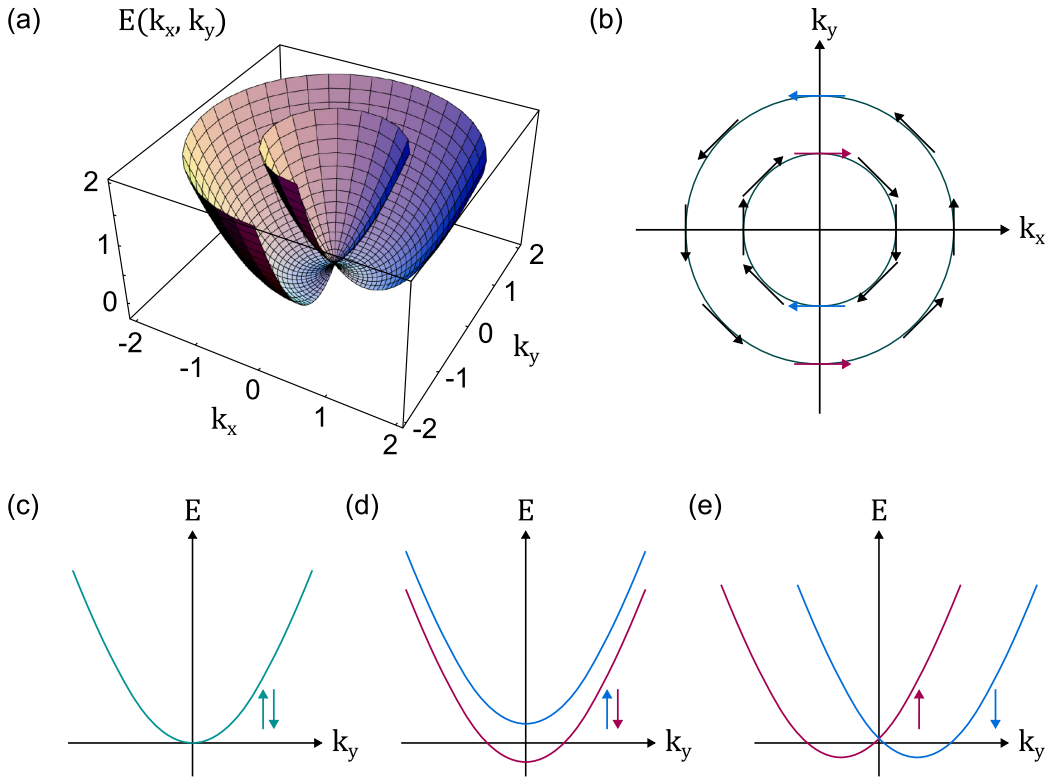

Figure 2.3: *Spin splitting in the energy spectrum of a free electron in a 2DEG due to Rashba SOC.* ***(a)*** *Part of the Rashba energy spectrum in 2D k-space.* ***(b)*** *Iso-energy cut of (a) showing the Fermi contours with spin direction: electrons moving with opposite momentum have opposite spins. The red arrows correspond to the red parabolas in (d) and (e), likewise for the blue arrows and parabolas.* ***(c)*** *Energy spectrum along k_y without SOC.* ***(d)*** *Energy spectrum along k_y in an external magnetic field; Zeeman splitting.* ***(e)*** *Energy spectrum along k_y in the presence of Rashba SOC, where lack of spatial inversion symmetry lifts the spin-degeneracy. Image adapted from [27].*

2.2.1 SOC as long-range triplet source

While magnetic inhomogeneity forms the basis of essentially all current methods of LRTC generation, it has also been proposed that (Rashba) SOC can be used for singlet-triplet conversion instead [15, 16, 30, 31]. In this section we discuss a theoretical description of SOC as a source for the LRTC as developed by Bergeret and Tokatly [15]. We refer to Ref.[15] for any details.

The basis of the theory is formed by the analogy of spin diffusion in a normal metal with SOC (N_{SOC}) and singlet-triplet conversion in a diffusive S/F_{SOC} system. In the N_{SOC} system, Bergeret and Tokatly [15] incorporate the SOC vector potential $\hat{\mathcal{A}}_k = \frac{1}{2}\mathcal{A}_k^a\sigma^a$ (σ^a denotes the Pauli matrices) in the diffusion equation by replacing the derivatives by their covariant counterparts, $\partial_k\cdot \mapsto \tilde{\nabla}_k\cdot = \partial_k \cdot -i[\hat{\mathcal{A}}_k, \cdot]$, on the basis of gauge invariance arguments. The spin diffusion equation in terms of the spin-density vector $\mathbf{S} = (S^x, S^y, S^z)$ is then given by Equation (2.8) for a normal metal with linear in momentum SOC.

$$\partial_t S^a = D\nabla^2 S^a + 2C_k^{ab}\partial_k S^b - \Gamma^{ab}S^b \tag{2.8}$$

S^a denotes the components of the spin-density vector and D is the diffusion constant. The two terms with the tensors C_k^{ab} and Γ^{ab} (a, b refer to spin, k to momentum) are a direct result of the SOC and provide two possible mechanisms for spin rotation in the normal metal.

The first mechanism is possible anisotropy in the spin relaxation tensor Γ^{ab}. Spin rotation occurs because the spin relaxes more slowly along the principal axes of Γ^{ab}, and an injected spin that is not parallel to one of the principal axes will therefore turn towards this direction. The second mechanism, driven by C_k^{ab}, originates from a spin density inhomogeneity along the direction k that induces a spin precession around the direction of inhomogeneity. The definitions for C_k^{ab} and Γ^{ab} are given by Equations (2.9) and (2.10),

$$C_k^{ab} = D\varepsilon^{acb}\mathcal{A}_k^c \tag{2.9}$$

$$\Gamma^{ab} = D(\mathcal{A}_k^c\mathcal{A}_k^c\delta^{ab} - \mathcal{A}_k^a\mathcal{A}_k^b) \tag{2.10}$$

where ε^{acb} is the Levi-Civita tensor. From Equation (2.10) we can see that Γ^{ab} is quadratic in $\mathcal{A}$, as it follows from the $\partial_k\cdot \mapsto \tilde{\nabla}_k$ replacement that causes a double commutator in the diffusion equation. The effect of spin

relaxation anisotropy on spin rotation is therefore smaller than the precessional term with C_k^{ab}. An important requirement for the spin precession, however, is that there must be a spatial component of the SOC $\mathcal{A}_k^c$ along the direction of the inhomogeneity that induces the precession.

Now moving to superconducting systems, an equation similar to Equation (2.8) is derived for a diffusive S/F$_{\text{SOC}}$ structure. Taking the linearized Usadel equation as a starting point to describe the superconducting condensate in F, Bergeret and Tokatly [15] again modify it to include linear in momentum SOC by replacing $\partial_k \cdot \mapsto \tilde{\nabla}_k \cdot = \partial_k \cdot -i[\hat{\mathcal{A}}_k, \cdot]$. Furthermore, using $\hat{f} = f_s \hat{1} + f_t^a \sigma^a$ to represent the condensate function with a singlet component f_s and triplet components f_t^a, Equations (2.11) and (2.12) describe the spatial distributions of the singlet and triplet components in F$_{\text{SOC}}$.

$$D\nabla^2 f_s - 2|\omega| f_s - 2i\,\mathrm{sgn}(\omega) h^a f_t^a = 0 \tag{2.11}$$

$$D\nabla^2 f_t^a + 2C_k^{ab}\partial_k f_t^b - \Gamma^{ab} f_t^b - 2|\omega| f_t^a - 2i\,\mathrm{sgn}(\omega) h^a f_s = 0 \tag{2.12}$$

With ω the Matsubara frequency and h^a a component of the ferromagnetic exchange field $\hat{h} = h^a \sigma^a$. In Equation (2.12) we recognize the tensors C_k^{ab} and Γ^{ab} that are responsible for the spin rotation that results in singlet-triplet conversion. At the S/F$_{\text{SOC}}$ interface, a triplet component appears that is parallel to the exchange field direction and which decays over the short-range length scale $\xi_h \propto \sqrt{D/h}$. Analogous to the case of SOC in a normal metal, the condensate spin rotates in the course of diffusion due to the SOC and this creates a component of the condensate spin that is perpendicular to the exchange field — the LRTC.

LRTC in transversal and lateral geometries

SOC can therefore generate the LRTC in the absence of magnetic inhomogeneity, but for practical use of this theory we must also consider the geometry of the system. In many experimental applications the SOC-mediated LRTC would be generated and tested in Josephson junctions that have either a *transversal* or a *lateral* geometry depending on how the different materials are stacked (see Figure 2.4). Bergeret and Tokatly [15, 16] show that the requirements for singlet-triplet conversion in a transversal junction are more restrictive, a result that is of practical importance in this work.

Version of October 13, 2025– Created October 13, 2025 - 11:10

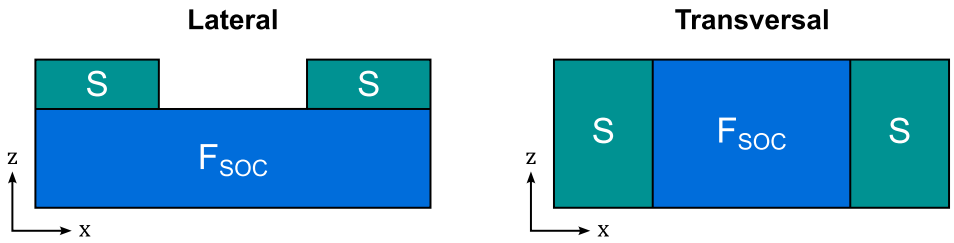

Figure 2.4: *The lateral (left) and transversal (right) junction geometries. In the lateral geometry the interfaces are in the (x, y)-plane and the condensate function varies in x and z due to translational invariance in y. In the transversal geometry the interfaces are in the (y, z)-plane and the condensate varies only in x.*

In the treatment of the transversal and lateral geometries, the crucial difference lies in the direction of inhomogeneity in the condensate $\hat{f}$ in combination with the SOC. Spatial asymmetry defines the direction of the inhomogeneity and, if we assume *only* Rashba SOC, for its relevance in this work, it also defines the spatial components of the SOC. Focusing on the lateral junction in Figure 2.4 first, there is translational invariance only in the y-direction (assuming infinite dimensions in y) and the condensate can therefore vary in x and z. Due to the $\mathrm{S/F_{SOC}}$ interfaces in (x, y), the Rashba SOC vector potential has components $\mathcal{A}^x_y$ and $\mathcal{A}^y_x$, coupling spin in x to momentum in y and vice versa. The requirement for spin precession driven by C^{ab}_k is therefore fulfilled, since C^{ab}_k and the inhomogeneity in $\hat{f}$ both have components in x. Moreover, the diffusive spin precession tensor C^{ab}_k is dominant over Γ^{ab} due to practical considerations: in a realistic ferromagnet, the direction of the exchange field and one of the principal axes of Γ^{ab} likely coincide because both are linked to the crystal structure, in which case Γ^{ab} does not sufficiently contribute to the singlet-triplet conversion. Thus, in the lateral geometry, a pure Rashba SOC at the $\mathrm{S/F_{SOC}}$ interface can generate the LRTC for an *arbitrary* exchange field direction, due to the spin precession mechanism.

In a transversal junction the singlet-triplet conversion is less universal. In Figure 2.4 we can assume that the condensate is translationally invariant in both y and z, thus the condensate function only depends on x. Furthermore, the Rashba SOC vector potential has components $\mathcal{A}^y_z$ and $\mathcal{A}^z_y$ due to the interfaces in the (y, z)-plane. As a result, the spin precession mechanism does *not* contribute to spin rotation since the inhomogeneity in $\hat{f}$ is in x and there is no $\hat{\mathcal{A}}_x$ component. The LRTC can therefore only be generated from anisotropy in Γ^{ab}, which poses the condition that the exchange

field $h^a\sigma^a$ is *not parallel* to the vector $[\hat{\mathcal{A}}_k, [\hat{\mathcal{A}}_k, h^a\sigma^a]]$. If we assume a pure Rashba SOC, $[\hat{\mathcal{A}}_k, [\hat{\mathcal{A}}_k, h^a\sigma^a]]$ is expressed by Equation (2.13).

$$[\hat{\mathcal{A}}_k, [\hat{\mathcal{A}}_k, h^a\sigma^a]] = 4\alpha_R^2(2h^x\sigma^x + h^y\sigma^y + h^z\sigma^z) \tag{2.13}$$

Importantly, the factor 2 in the $h^x\sigma^x$ term makes the LRTC possible at all with pure Rashba SOC in the transversal geometry. If $h^x \neq 0$, and $h^y \neq 0$ and/or $h^z \neq 0$, the LRTC is generated because the vector in Equation (2.13) will not be parallel to $\hat{h} = h^a\sigma^a$. However, a pure Rashba SOC cannot generate the LRTC in a transversal junction if the exchange field is simply in-plane ($h^x = 0$), which is generally the most common.

In summary, a pure Rashba SOC does not easily generate the LRTC since the spatial asymmetry that causes the Rashba SOC simultaneously causes the condensate inhomogeneity *perpendicular* to the vector potential components of the Rashba SOC. We also note that in their treatment of the lateral geometry, which in Ref.[15] is actually S/F_{SOC}/F with the F layer extending in the x-direction, Bergeret and Tokatly [15] assume the S and F_{SOC} layers to be thin enough that the condensate $\hat{f}$ does not vary in z within these layers. A proper analysis of the z-direction (perpendicular to the interface) in the lateral geometry is therefore lacking, since the spin rotation must take place in the F_{SOC} layer. As a final remark, ferromagnets with high intrinsic SOC generally do not exist and have to be fabricated as alloys [32, 33] or using heavy metal/ferromagnet interfaces [11, 14], and in many cases the SOC is then Rashba-type, as it is in this work too.

Version of October 13, 2025– Created October 13, 2025 - 11:10

Chapter 3

Proximity effects in Nb, Pt and Co bilayers

At the interface between a superconductor and normal metal, some of the superconductivity 'leaks' into the metal over a length that is characterized by ξ_N (see Section 2.1), but this proximity effect also includes the partial depletion of Cooper pair density in the superconductor over a length ξ_S near the interface. If the superconducting layer thickness is of the order of ξ_S this reduced Cooper pair density can be measured as a reduction in T_c.

In this chapter, we make thin film bilayers of Nb on Pt and/or Co and measure their T_c. By comparison of Nb/Co, Nb/Pt/Co and Nb/Pt samples we comment on the effect of a Pt interlayer on the proximization of the Co (Section 3.2). In addition, we measure the temperature dependencies of the upper critical field of the films, both in-plane (IP) and out-of-plane (OOP) to determine the coherence length and dimensionality of the superconducting layer (Section 3.3).

3.1 Sample fabrication

An overview of the sample fabrication process and the different samples is given in Figure 3.1. The fabrication process consists of electron-beam lithography (EBL) and thin film deposition to create lift-off structures whose transport properties can be measured with a four-probe Van der Pauw method.

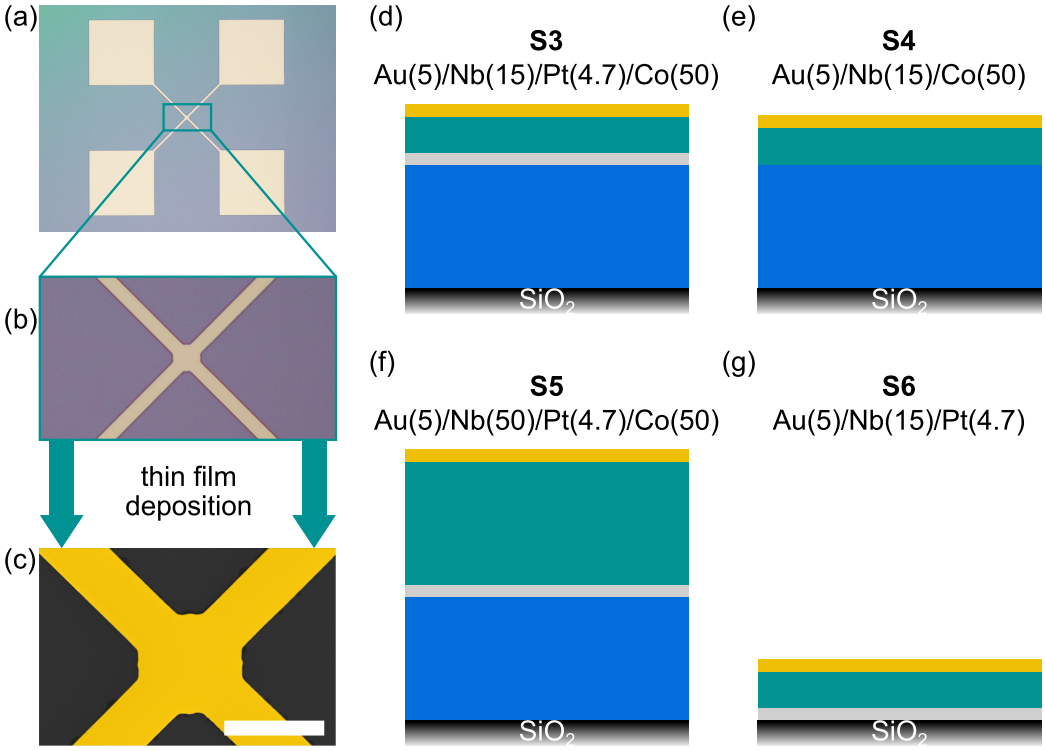

Figure 3.1: *Overview of the thin film sample fabrication.* ***(a)*** *A design for a four-probe measurement of a* 20 µm×20 µm *square (zoom in* ***(b)****) is patterned with EBL. The large squares in (a) are* 300 µm×300 µm*.* ***(c)*** *Scanning electron micrograph (false-colored) of a structure after sputtering and lift-off. The scale bar indicates* 20 µm*.* ***(d)-(g)*** *Four samples were produced, each with different combinations of Pt and/or Co layers. The layer thicknesses (parentheses, in* nm*) in the schematic drawings are to scale w.r.t. one another. Sample S5 was made with* 50 nm *Nb, as a reference to the samples in Chapter 4.*

3.1.1 Electron-beam lithography

We use EBL to write a pattern for a 20 µm×20 µm square with four 300 µm×300 µm contact pads for wire bonding. Each sample chip contains 8 such structures. Diced 0.5 mm thick Si wafers with 300 nm thermal oxide are used as substrates and are thoroughly cleaned in acetone with an ultrasonic bath for 10 min and rinsed with isopropyl alcohol (IPA). We spin coat at 4000 rpm with one layer of polymethyl methacrylate (PMMA) 600K positive resist (AR-P 662.06), followed by one layer of PMMA 950K (AR-P 672.045). The 600K resist has a lower molecular mass and is therefore more sensitive than the 950K resist, creating an undercut for easier lift-off. The sample is baked on a hot plate at 180 °C for 3 min after each resist layer.

Version of October 13, 2025– Created October 13, 2025 - 11:10

We use a Raith 100 EBPG to pattern the design with a 350 µC cm^{-2} dose. Following the exposure, we develop the patterned sample in a 1:3 solution MIBK:IPA for 45 s, dissolving the exposed resist, before stopping the reaction in pure IPA. Figure 3.1 (a) shows an optical image of a developed structure, and the 20 µm×20 µm square can be seen at higher magnification in Figure 3.1 (b).

3.1.2 Thin film deposition

The Co, Pt and Nb layers are deposited on the sample with dc magnetron sputtering in an ultra-high vacuum (UHV) system. The chamber pressure prior to sputtering was 4.0×10^{-10} mbar for S3, S4 and S5, and 3.2×10^{-10} mbar for S6. An Ar pressure of 4.0×10^{-3} mbar is maintained during the sputtering process. For S6, which does not have Co, we confirmed with atomic force microscopy (AFM) that 4.7 nm sputtered Pt forms a uniform film on a thermal oxide Si substrate. To prevent oxidation of the Nb layer, which is sputtered last, the samples are quickly transferred to a modified Leybold-Heraeus Z400 dc sputtering machine with a base pressure $<1 \times 10^{-5}$ mbar to sputter a 5 nm Au capping layer at 4.9×10^{-3} mbar Ar pressure. This Au layer will also become proximized when the sample cools down and becomes superconducting, which will also reduce T_c, but its thickness is the same for all samples.

After film deposition, we perform lift-off by leaving the sample in acetone overnight and then put this in an ultrasonic bath (at 50%) for a few seconds. We finish by rinsing the sample in IPA and drying with a nitrogen spray gun. See Figure 3.1 (c) for a scanning electron micrograph of a finished structure after lift-off.

Layer thicknesses

We choose our layer thicknesses to be 50 nm for Co, 4.7 nm for Pt and 15 nm for Nb. The Nb thickness is especially important, since a thinner layer will show a greater difference in T_c due to the proximity effect, but a layer too thin will not become superconducting. We estimate that 15 nm is an appropriate thickness for the Nb in our bilayer samples, based on work by Koorevaar, Coehoorn, and Aarts [34] on V/Co *multilayers*. They found a critical thickness of 23 nm for the V layer, which must be of the order $2\xi_{GL}(0)$ in multilayers, and a zero-temperature Ginzburg-Landau coherence length $\xi_{GL}(0) = 12.3$ nm, a value similar to $\xi_{GL}(0)$ for Nb [20, 22].

The samples S3, S4, S5 and S6 are shown in Figure 3.1 (d)-(g). S3 is the sample where Pt is used as a thin interlayer between the Nb and Co. We wish to determine the effect of the Pt interlayer from comparison with samples S4 and S6, which respectively lack either the Pt or the Co. The main purpose of sample S5 is to compare its T_c with the T_c of the bulk Nb in the evaporated junction devices in Chapter 4. S5 has 50 nm Nb on Pt and Co and its layers are therefore similar to the junction devices.

3.2 Critical temperatures

To determine the critical temperature of each sample, we measure the resistance R as a function of temperature T. The four-probe resistances are measured in a horizontal Van der Pauw configuration (see Figure 3.2 (b)) and the samples are cooled down in a Quantum Design DynaCool-9T PPMS cryostat. A Keithley current source (6221) and nanovoltmeter (2182A) are used to apply a current bias and measure $R = \frac{V(100\mu A) - V(-100\mu A)}{200\mu A}$. We define the critical temperature T_c as the temperature where $R = 0.5R_N$, R_N indicating the normal-state resistance. For our sample with 50 nm Nb (S5) we find $T_c = 7.8$ K. This is a common value for sputtered Nb in our lab and it is slightly higher than the $T_{c,Nb}$ of the evaporated devices in Chapter 4. Therefore we also assume good Nb quality in samples S3, S4 and S6.

The $R(T)$ measurements for samples S3 (Au/Nb/Pt/Co), S4 (Au/Nb/Co) and S6 (Au/Nb/Pt) are presented in Figure 3.2 (a). A first result is that the critical temperatures of the Au/Nb/Co and Au/Nb/Pt films are quite close to one another but Au/Nb/Co has the slightly higher T_c, with $T_{c,S4} = 6.2$ K and $T_{c,S6} = 5.7$ K respectively. This is rather unexpected, since the exchange field of Co is a strong pair-breaking mechanism while the high SOC in Pt by itself does not necessarily break Cooper pairs because it respects time reversal symmetry. Furthermore, the T_c of Au/Nb/Pt may be lowered by the proximity effect, but Pt has a short coherence length (we estimate $\sim$10 nm based on Ref.[18]) and the Pt layer is only 4.7 nm thick, so one would still expect a lower T_c for Au/Nb/Co. We do note that the superconducting transition in Au/Nb/Co is rather broad, ~ 0.6 K, which suggests that there is more inhomogeneity in the film compared to the other samples. The thin Nb, sputtered at a 45° angle, possibly grows less uniform on Co than on Pt. The higher normal-state resistance of the Au/Nb/Pt sample is due to the total thickness of the film that is only approximately 1/3 of the total thickness of each of the other samples.

Version of October 13, 2025– Created October 13, 2025 - 11:10

Most notably, sample S3 with both Pt *and* Co has a significantly lower critical temperature $T_{c,S3} = 3.5\,\mathrm{K}$. The difference with samples S4 and S6 is more than 2 K, which constitutes a 39% T_c-reduction compared to S6 and 44% compared to S4. The physical cause of the low T_c is ambiguous, however. From a possible SOC-generated LRTC point of view, it is thinkable that the SOC introduced by the Pt converts a portion of the condensate into the LRTC that can leak into the Co, thereby depleting the Nb of Cooper pairs and lowering T_c. In this interpretation the pair-breaking effects of the exchange field are also responsible for part of the T_c suppression. Alternatively, the combination of SOC and exchange field might enhance pair-breaking in S3, although it has also been proposed that SOC can protect against pair-breaking from Zeeman fields or exchange fields [35, 36]. A T_c-reduction may also be explained by an increase in interface transparency. It has been measured in S/F multilayers with alloys that a reduced magnetic moment of F increased the transparency of the interface, resulting in lower T_c [37].

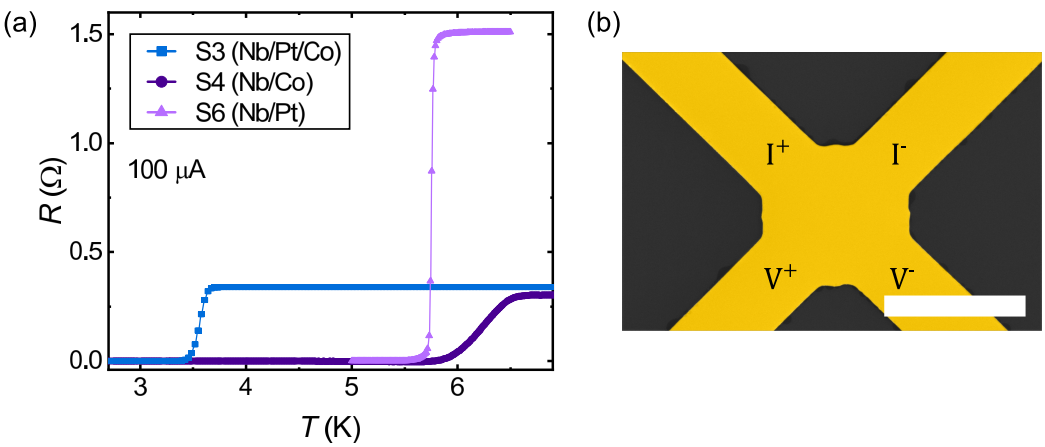

Figure 3.2: *$R(T)$ measurements of the superconducting transitions of samples S3 (Au/Nb/Pt/Co), S4 (Au/Nb/Co) and S6 (Au/Nb/Pt), measured at a* 100 µA *current.* ***(b)*** *Scanning electron micrograph (false-colored) indicating the I^+/I^- and V^+/V^- contacts for the four-probe Van der Pauw configuration.*

In a way, the Au/Nb/Pt and Au/Nb/Co samples represent the extremas of varying the Pt thickness in Au/Nb/Pt/Co: in its thin limit, the Pt layer approaches 0 nm, equivalent to Au/Nb/Co. Meanwhile, a very thick Pt layer (much thicker than ξ_{Pt}) would fully shield off the Co from the superconducting condensate and resemble Au/Nb/Pt. One can therefore imagine that there exists some Pt layer thickness for which T_c is minimal.

Version of October 13, 2025– Created October 13, 2025 - 11:10

Admittedly, the 4.7 nm Pt in our Au/Nb/Pt sample is not in the 'thick limit' since a partial gap in 10 nm Pt on Nb has been measured with scanning tunneling spectroscopy [18]. A Au/Nb/Pt sample with much thicker Pt would be required to support this rather speculative argument, as well as Au/Nb/Pt/Co samples with varying Pt thicknesses.

3.3 Upper critical fields

We measure the upper critical fields of our films to estimate the zero-temperature coherence length $\xi(0)$ and find if the film can be described by the 2D limit of the Ginzburg-Landau model, as another way to probe the proximity effect. $\xi(0)$ can be calculated from the slope of the upper critical field H_{c2} as function of the temperature T, evaluated near T_c. In our thin films, we use the OOP H_{c2}, given by Equation (3.1), to determine this slope.

$$H_{c2}^{OOP}(T) = \frac{\Phi_0}{2\pi\xi^2(0)}(1 - T/T_c) \tag{3.1}$$

Φ_0 denotes the magnetic field quantum. We differentiate Equation (3.1) w.r.t. T to find the slope near T_c, given by Equation (3.2).

$$\left.\frac{dH_{c2}}{dT}\right|_{T=T_c} = -\frac{\Phi_0}{2\pi\xi^2(0)T_c} \tag{3.2}$$

When the thickness d of a superconducting thin film is smaller than the coherence length, the IP upper critical field H_{c2}^{IP} of the film can be much larger than H_{c2}^{OOP} because it does not have much diamagnetic energy to generate the OOP orbital screening currents in comparison to a bulk superconductor. In the 2D limit, the upper critical field is therefore dependent on the *effective* thickness d_{eff} of the superconductor (Equation (3.3)) [38]:

$$H_{c2}^{IP}(T) = \frac{\sqrt{3}\Phi_0}{\pi d_{eff}\xi(0)}\sqrt{1 - T/T_c} \tag{3.3}$$

A key difference between the expressions in Equation (3.1) and Equation (3.3) is the power of $\xi(0)$. The temperature dependence of the coherence length is $\xi(T) \propto 1/\sqrt{1 - T/T_c}$ (Equation (2.3)). For this reason, the temperature dependence of H_{c2} in 3D is $\propto (1 - T/T_c)$, while in the 2D limit $H_{c2} \propto (1 - T/T_c)^{1/2}$. Hence, we can use Equation (3.4) as a general equation to describe H_{c2} with α as a measure for the dimensionality of the thin films.

$$H_{c2}(T) = H_{c2}(0\,\mathrm{K})(1 - T/T_c(0\,\mathrm{T}))^{\alpha} \tag{3.4}$$

Version of October 13, 2025– Created October 13, 2025 - 11:10

Here, $H_{c2}(0\ \mathrm{K})$ is the zero-temperature upper critical field and $T_c(0\ \mathrm{T})$ is the zero-field critical temperature.

To obtain our data we measure the four-probe resistance of a sample as in Section 3.2 while varying the (IP or OOP) externally applied magnetic field $\mu_0 H$ in steps of a few tens of mT over a field range in which the superconducting transition occurs. This type of measurement results in a sigmoid-shape $R(\mu_0 H)$ curve and we perform such a measurement for ∼20 different temperatures below and up to $T_c(0\ \mathrm{T})$ (as measured in Section 3.2). The upper critical field at each temperature is chosen where $R = 0.5R_N$. We fit these data points to Equation (3.4) using $H_{c2}(0\ \mathrm{K})$, $T_c(0\ \mathrm{T})$ and α as fitting parameters, where α provides insight into the 2D or 3D behavior of our samples [20]. Figure 3.3 (a) shows the results for OOP field , the results for IP field are presented in Figure 3.3 (b).

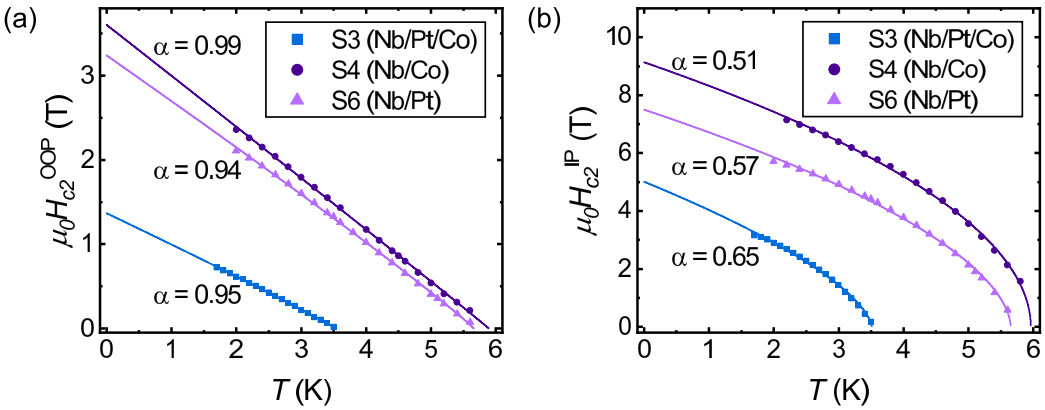

Figure 3.3: *Upper critical field $\mu_0 H_{c2}$ as function of temperature for* ***(a)*** *out-of-plane field, and* ***(b)*** *in-plane field. α indicates the power of the temperature dependence $(1 - T/T_c)^{\alpha}$. Dots indicate the experimental data points and solid lines show the results of fitting the data to Equation* (3.4).

Focusing on $H_{c2}^{OOP}(T)$ first, we find that it is approximately linear for all three samples, following Equation (3.1) as expected from the large lateral dimensions (20 µm×20 µm) of the films. It is unclear why the two samples with Pt (S3 and S6) have slightly lower α^{OOP}, however. We find $dH_{c2}^{OOP}/dT\big|_{T=T_c} = -0.40, -0.60$ and -0.57 for S3, S4 and S6, respectively, and calculate $\xi(0)$ to be 15.3 nm for S3, 9.6 nm for S4 and 10.1 nm for S6. We thus find that the coherence length is more than 50% larger in the sample with both Pt and Co, compared to only Pt *or* Co. However, we must note that this is not an entirely fair comparison, since the condensate de-

Version of October 13, 2025– Created October 13, 2025 - 11:10

pletion in S4 (Nb/Co) is not from superconducting proximity but from Cooper pair breaking, which limits the conclusions we can draw from its calculated $\xi(0)$. An overview of the T_c and α fitting parameters and calculated $\xi(0)$ can be found in Table 3.1.

Next, the parameter α^{IP} from the fits to the $\mu_0 H_{c2}^{IP}(T)$ data informs us of the dimensionality of our films. With $\alpha^{IP} = 0.51$ we can conclude that the Au/Nb/Co sample is in the 2D limit, whereas the other two films are in the intermediate regime between 2D and 3D. For the Au/Nb/Pt sample it may be that $\alpha^{IP} > 0.5$ because of the condensate leaking into the 5 nm Au capping layer. Robbins *et al.* [20] have also investigated the upper critical fields of (*inter alia*) Au/Nb/Au and Pt/Nb/Pt (with $d_{Au,Pt} = 15$ nm and $d_{Nb} = 25$ nm), and found $\alpha^{IP} = 0.70$ for Au and $\alpha^{IP} = 0.50$ for Pt. Similarly, the Au capping may be partly responsible for $\alpha^{IP} = 0.65$ in the Au/Nb/Pt/Co sample, but there is possibly also some other physics in play to explain the difference with the other samples.

	T_c^{OOP} (K)	α^{OOP}	T_c^{IP} (K)	α^{IP}	$\xi(0)$ (nm)
S3 (Nb/Pt/Co)	3.53 ± 0.01	0.95 ± 0.01	3.51 ± 0.01	0.65 ± 0.01	15.3 ± 0.1
S4 (Nb/Co)	5.89 ± 0.03	0.99 ± 0.02	5.96 ± 0.03	0.51 ± 0.02	9.6 ± 0.1
S6 (Nb/Pt)	5.66 ± 0.02	0.94 ± 0.02	5.65 ± 0.02	0.57 ± 0.02	10.1 ± 0.1

Table 3.1: *Overview of the best fitting parameters T_c and α to Equation* (3.4) *for the OOP and IP data of S3, S4 and S6. The last column indicates the zero-temperature coherence length $\xi(0)$ that is calculated from $H_{c2}^{OOP}(0\,\mathrm{K})$ using Equation* (3.1).

In summary, the Au/Nb/Pt/Co sample displays behavior that strongly deviates from the samples that only contain Pt *or* Co, in terms of its T_c, $\xi(0)$ and dimensionality. The behavior could be due to SOC-mediated LRTC generation, which may explain the low T_c as the leakage of equal-spin triplets into the Co, likely in addition to pair-breaking of a fraction of the singlets and short-range triplets. This explanation could also account for the much longer $\xi(0)$ and least 2D-like behavior. However, we lack direct evidence of equal-spin triplets. Additionally, the geometry of the thin film samples best resembles the transversal geometry with in-plane mag-

Version of October 13, 2025– Created October 13, 2025 - 11:10

netization as treated theoretically by Bergeret and Tokatly [15], a geometry in which Rashba SOC alone would not produce the LRTC.

Chapter 4

Junctions in Nb/Pt/Co devices

In this chapter, we describe the fabrication and properties of lateral junction devices that could potentially provide direct evidence of SOC-generated equal-spin triplets. We intend to create lateral Nb/Pt/Co/Pt/Nb junctions through which singlet and $m_s = 0$ triplet transport is impossible. Measuring a supercurrent through such a junction would prove the LRTC that would be generated from the Rashba SOC at the interface with Pt. Section 4.1 describes the fabrication process of the devices and we report on the T_c and field dependence in Section 4.2. Section 4.3 discusses if our junctions are of the type Nb/Pt/Co/Pt/Nb with additional measurements.

4.1 Device fabrication

The bar-shaped devices with junctions, an example (dev.1a) shown in Figure 4.1 (a)-(b), are samples that we fabricated similar to S5 in Chapter 3 (Figure 3.1 (c)), apart from the deposition process and additional focused ion beam (FIB) milling. We use Ga^+ FIB to create the 1 µm×5 µm bar structure and separate the four contacts (Figure 4.1 (a)), and we cut a trench into the middle of the bar for our Josephson junction (Figure 4.1 (b)). In total, we made four devices in two different samples, two devices on each sample, as shown in the overview in Figure 4.1 (c)-(f). The two samples (S1 and S2) differ in the thickness of their Pt layers, and the two devices on a sample differ in the depth of their trenches. The naming convention of devices 1a, 1c (on sample S1), 2a, 2b (on sample S2) is based on the fact that samples S1 and S2 each contain 10 structures that can be made into devices with FIB, that we denote by a letter a-j from the top left to the bottom right.

Version of October 13, 2025– Created October 13, 2025 - 11:10

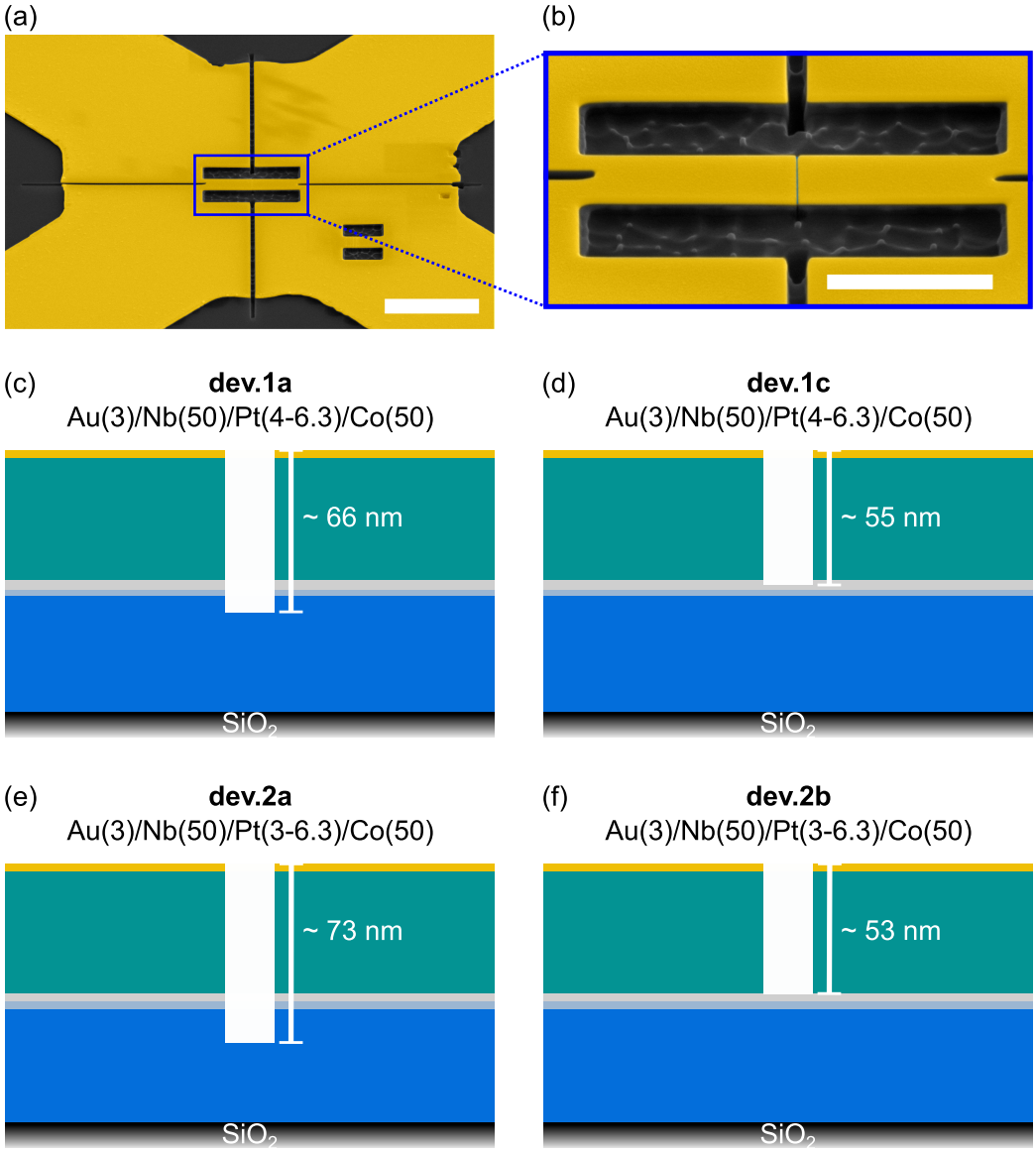

Figure 4.1: *Overview of the junction devices.* ***(a)*** *Scanning electron micrograph (false-colored) of the bar-shaped device centered in a* 20 µm×20 µm *square of deposited material. The small bar in the bottom right functioned as a dose test for FIB milling. The scale bar indicates* 5 µm. ***(b)*** *Close-up of the bar with the junction. The scale bar indicates* 2 µm. ***(c)-(f)*** *The four devices that were fabricated, consisting of (top to bottom) Au, Nb, Pt and Co on* SiO_2*. Numbers in parentheses indicate layer thicknesses in* nm*. There is some uncertainty in the Pt layer thicknesses, see Section 4.1.1. Devices 1a (c) and 1c (d) have thicker Pt than 2a (e) and 2b (f). Devices 1a and 2a have deeper trenches than 1c and 2b.*

The first step in the fabrication of the junction devices is EBL, exactly as described for the bilayer film samples in Section 3.1. For the thin film deposition, however, we use electron-beam evaporation (Plassys MEB600SL) with base pressure $<5 \times 10^{-8}$ mbar to evaporate 50 nm Co, a few nm Pt, 50 nm Nb and 3 nm Au. A quartz crystal microbalance (QCM) monitors the thickness of the evaporated film. Since the Au capping layer can also be evaporated *in situ*, the Nb need not be exposed to air in this process. The lift-off procedure for the evaporated film is more gentle; a night in acetone and a rinse in IPA suffices without the need for any ultrasonication. A drawback to the evaporation of thin layers of Pt, which requires relatively high emission currents ($\sim$75 mA), is that heating of the QCM influences the calculated deposition rate. For very thin Pt films ($\sim<5$ nm), this means that the actual deposited film thickness may differ from the desired thickness. We elaborate on this problem, and our determination of its extent in our samples, in Section 4.1.1. After the deposition and lift-off, FIB milling is the final step in the fabrication process, which we describe in more detail in Section 4.1.2.

4.1.1 Thickness of evaporated Pt

The evaporation of Pt causes heating of the QCM, thereby changing its physical properties, such as a change in density due to thermal expansion. The deposition of Pt on the QCM can also create temperature gradients across the crystal's surface [39] that lead to thermal stress [40]. These thermal effects influence the resonance frequency f_0 of the QCM, which is used to calculate the deposition rate using the Sauerbrey equation (Equation (4.1)) [41, 42].

$$\Delta f = -\frac{2f_0^2}{A\sqrt{\rho_q \mu_q}}\Delta m \tag{4.1}$$

In the absence of thermal effects, the deposition rate that follows from the mass change Δm and the piezoelectrically active crystal area A can be directly calculated from the measured frequency change Δf, knowing the quartz's density ρ_q and shear modulus μ_q to be constant. However, at the start of the Pt evaporation process, the QCM heats up and the deposition rate as calculated from Equation (4.1) is less accurate. The resulting film thickness may deviate from the desired film thickness by only a few nm, but this can be problematic when one wants to deposit a film with the same order of thickness as this deviation.

For our devices we desire a Pt layer thickness of 4 nm (S1) and 3 nm (S2).

To determine the deviation from a 4 nm desired thickness, we made one 'calibration' sample. We first evaporated 15 nm Co and 4 nm Pt on a bare thermal oxide Si substrate. After that, we patterned with EBL an array of 10 µm×10 µm squares and evaporated another 4 nm Pt. After lift-off we measured the height of the squares with AFM and found an average thickness of 6.3 nm ± 0.3 nm (see Figure 4.2 (a)). Background subtraction in the AFM image was done using the line-by-line median of differences and three-point leveling of the substrate.

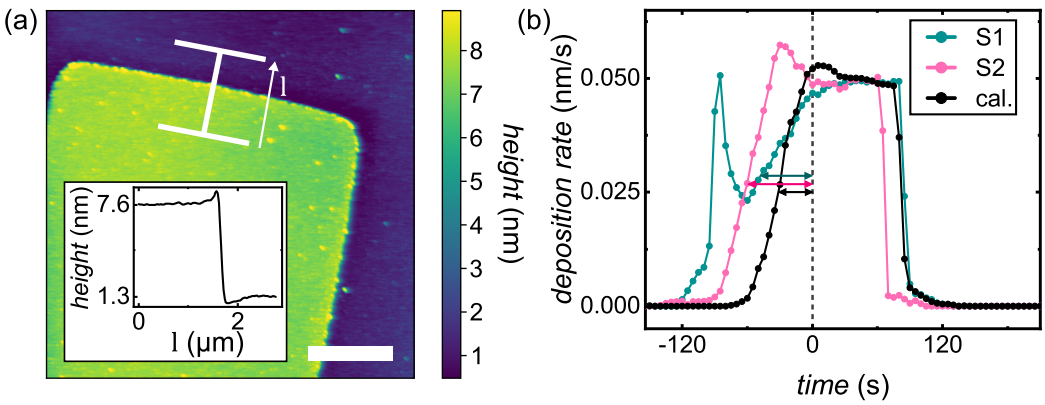

Figure 4.2: *The calibration sample for Pt evaporation.* ***(a)*** *AFM image of the calibration sample. The arrow indicates the direction of the averaged line measurement that is shown in the inset. The scale bar indicates* 3 µm. ***(b)*** *Deposition rates during the Pt evaporation processes of samples S1, S2 and the calibration sample (cal.). The time between the start of evaporation and the opening of the shutter at* $time = 0$ *is the shortest for the calibration sample, as indicated by the arrows.*

To argue that 6.1 nm is an upper limit for the Pt layer thickness in both samples S1 and S2, we compare the Pt evaporation processes of S1, S2 and the calibration (cal.) sample in Figure 4.2 (b). We can see that the time between the start of evaporating material ($deposition\ rate > 0$) and opening the shutter (at $time = 0$ s, dashed vertical line) is the shortest for the calibration sample. In other words, during the Pt evaporation process of the calibration sample the QCM has the least amount of time to reach a stable temperature before the start of material deposition on the sample. Thus we conclude that the deviation from the desired Pt thickness is largest in the calibration sample. The Pt thickness in S1 is therefore between 4 nm and 6.3 nm, and in S2 between 3 nm and 6.3 nm. It is reasonable to assume that the Pt in S2 is thinner than in S1, as desired, but we do not have a separate upper limit.

Version of October 13, 2025– Created October 13, 2025 - 11:10

4.1.2 Focused ion beam milling

We structure our devices in an Aquilos 2 Cryo-FIB. To create the 1 µm-×5 µm bar in the center[1] of the 20 µm×20 µm square, we mill away two rectangles spaced 1 µm apart, all the way through the deposited films, using a 30 pA beam current. Four line cuts to the edges of the square allow for a four-probe measurement of the bar. With a 1.5 pA beam current, we cut a trench in the middle of the bar, perpendicular to its long axis. The trench is typically ∼20 nm wide and we intend it to be at least ∼60 nm deep, because we wish to fully cut through the Au, Nb and Pt layers.

The way we obtain an estimate for the trench depth in all devices in this work is shown in Figure 4.3: we determine the cross-sectional depth of the cut at the edge of the bar (under a 52° tilt angle). This method of trench depth determination is not very accurate, since the trench is generally deeper at the edges, so our reported trench depths hold most value in comparison of the different devices. For that reason the trenches in dev.1c and 2b are purposefully cut less deep, with the intent to have *not* reached the Co. That way, both S1 and S2 each have one device with a 'deeper' trench (dev.1a and 2a) and a 'less deep' trench (dev.1c and 2b). Measurements might show differences between the 'deeper' and the 'less deep' trench that could indicate if the 'deeper' trench has cut into the Co.

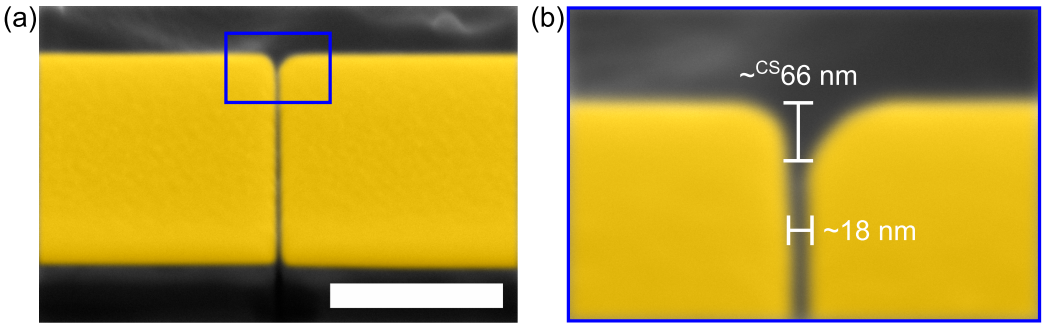

Figure 4.3: *Scanning electron micrograph (false-colored) of the FIB trench that makes the junction of device 1a. The scale bar indicates* 500 nm. *The blue rectangle outlines the region of the close-up in* ***(b)*** *that shows the cross-sectional measurement of the trench depth (*66 nm*) at* 52° *tilt and a measurement of the trench width (*18 nm*).*

[1]We avoid the edges of the square, where the Nb is contaminated with organic material from the PMMA resist.

Version of October 13, 2025– Created October 13, 2025 - 11:10

4.2 Critical temperature and field dependence

We measure the superconducting properties of our devices with DC voltage measurements in a Quantum Design DynaCool-9T PPMS and an Oxford Instruments TeslatronCF, similar to the films in Chapter 3. The four-probe resistance is measured using a 10 µA current bias, $R = \frac{V(10\mu A) - V(-10\mu A)}{20\mu A}$.

Figure 4.4 presents the four-probe resistance R as a function of the temperature T for devices 1a and 1c in (a) and for 2a and 2b in (b) as measured in the PPMS system. Figure 4.4 (d) shows how the current and voltage contacts are applied. All devices show a first transition around $T_{c,Nb} \approx 7.5\,\mathrm{K}$, when the Nb becomes superconducting, which is only 0.3 K lower than the T_c of the sputtered bilayer film S5 (7.8 K) in Section 3.2. Below $T_{c,Nb}$, R slowly decreases from $0.3\,\Omega$ until the devices become fully superconducting ($R = 0$) at $T_{c,junction}$.

Regarding the influence of the trench depth on $T_{c,junction}$, both Figure 4.4 (a) and (b) clearly show a higher T_c for the device with the less deep trench (dev. 1c, 3.5 K; dev. 2b, 4.2 K) compared to the deeper trench devices (dev. 1a, 2.1 K; dev. 2a, 3.0 K). This is a very intuitive result, since a deeper trench in this device geometry moves the junction further from the Nb/Pt interface, from where the Cooper pair density reduces in accordance with the proximity effect. Closely related to this point, the trench depth can make the difference between an S/S′/S (contsriction junction), $S/N_{SOC}/S$ and $S/N_{SOC}/F/N_{SOC}/S$ junction. In the latter case, a superconducting device must generate the LRTC and we expect lower $T_{c,junction}$ because the loss of the singlet and short-range triplet components decreases the Cooper pair density further. Although we have estimates of the trench depth that would make devices 1a and 2a $S/N_{SOC}/F/N_{SOC}/S$ junctions, we cannot be certain from the RT measurements alone and the lower $T_{c,junction}$ for devices 1a and 2a can also be explained with a S/S′/S or S/N/S junction without the LRTC.

A second observation that immediately becomes clear from Figure 4.4 (a) and (b) is that the devices on sample S2 have higher $T_{c,junction}$ than the devices on S1. While we have already established that the trench depth influences the $T_{c,junction}$ and we do not know the accuracy of our trench depth estimate, we assume that the estimation of the trench depths is at least somewhat *consistent*. Therefore we attribute this observation to the other main difference between these samples, which is that S2 has a thinner Pt

Version of October 13, 2025– Created October 13, 2025 - 11:10

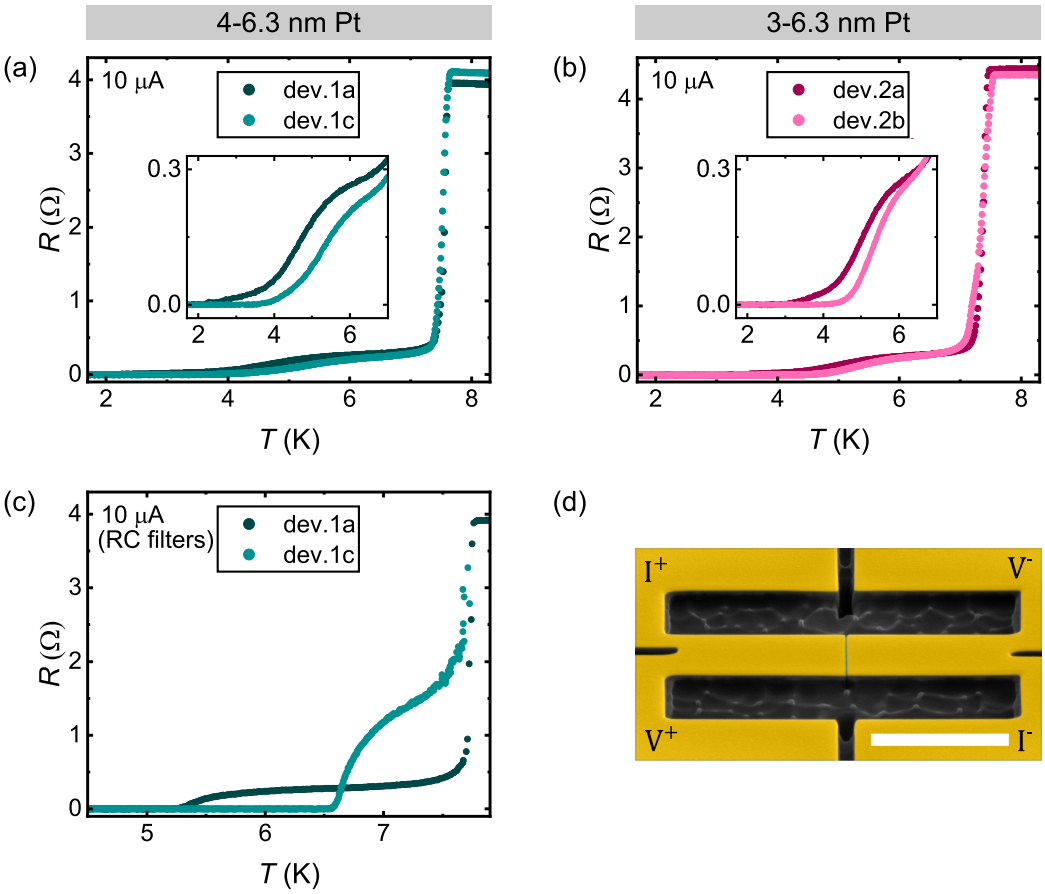

Figure 4.4: *Superconducting transitions of the devices on samples S1 (4 nm to 6.3 nm Pt, left) and S2 (3 nm to 6.3 nm Pt, right). Dark colors indicate deeper trenches (dev. 1a and 2a).* ***(a)*** *$R(T)$ of devices 1a and 1c, showing that dev. 1c becomes superconducting at higher T. The $R(T)$ data are all obtained using a 10 μA current.* ***(b)*** *$R(T)$ of devices 2a and 2b, showing that dev. 2b becomes superconducting at higher T.* ***(c)*** *$R(T)$ for devices 1a and 1c, but now measured in a system with RC filters. $R = 0$ at higher T compared to without the filters.* ***(d)*** *Configuration of the current (I^+/I^-) and voltage (V^+/V^-) contacts used for the four-probe R measurements.*

Version of October 13, 2025– Created October 13, 2025 - 11:10

layer. In light of the short coherence length ξ_{Pt} in Pt, a higher $T_{c,junction}$ is consistent with thinner Pt in the case of a Nb/Pt/Nb or Nb/Pt/Co/Pt/Nb junction. In the context of the possible SOC-mediated LRTC there is an additional consideration, however, in the sense that there could be an optimal Pt thickness, due to the competing LRTC generation and short ξ_{Pt}, as previously discussed by Satchell and Birge [10] and Jeon *et al.* [13]. In that case these results inform us that our Pt layers are thicker than optimal.

The $R(T)$ measurements are repeated for devices 1a and 1c in the Teslatron system two months later. This system is equipped with RC filters that eliminate rounding in $I(V)$ curves by reducing high frequency noise from thermal fluctuations, and so the transition to the superconducting state can be measured more sharply. For the junction devices this means that $R = 0$ is reached at higher temperatures than when measured in the PPMS system. The Teslatron $R(T)$ measurements are presented in Figure 4.4 (c) and we find for dev. 1a $T_{c,junction} = 5.2\,\mathrm{K}$ and for 1c $T_{c,junction} = 6.5\,\mathrm{K}$ (for unknown reasons, device 1c had higher resistance than before). We do note that the temperature reported in Figure 4.4 (c) is that of the variable temperature insert (VTI) since the sample temperature had not yet been properly calibrated. The $T_{c,Nb}$ for the Teslatron measurements is only 0.2 K higher than in the PPMS measurements, however, so we do not expect this deviation to be the main reason for the higher $T_{c,junction}$. The RC filters in the Teslatron insert therefore reveal that the devices 1a and 1c become fully superconducting at a temperature that is $\sim 2.8\,\mathrm{K}$ higher than in the PPMS measurements.[2]

Field dependence

Measurements of the field dependence of the critical current $I_c(\mu_0 H^{OOP})$, shown in Figure 4.5, confirm that we have junctions in all four of our devices through the presence of oscillations. These measurements were obtained from $I(V)$ curves at varying externally applied OOP magnetic field at $T \approx 0.8 T_{c,junction}$. The criterion $I_c = I(0.5\ \mu\mathrm{V})$ was chosen for the color scale cut-off. Interestingly, none of the $I_c(\mu_0 H^{OOP})$ patterns are the typical Gaussian or Fraunhofer forms that one would expect in a standard (diffusive or ballistic) S/S′/S or S/N/S junction. The pattern for device 1a is

[2]It should be noted that the same is *not* true for the bilayer films in Section 3.2. PPMS and Teslatron $R(T)$ measurements showed no difference in T_c for the films, just like the $T_{c,Nb}$ of the junction devices remains the same, apart from the difference in sample temperature and VTI temperature.

Version of October 13, 2025– Created October 13, 2025 - 11:10

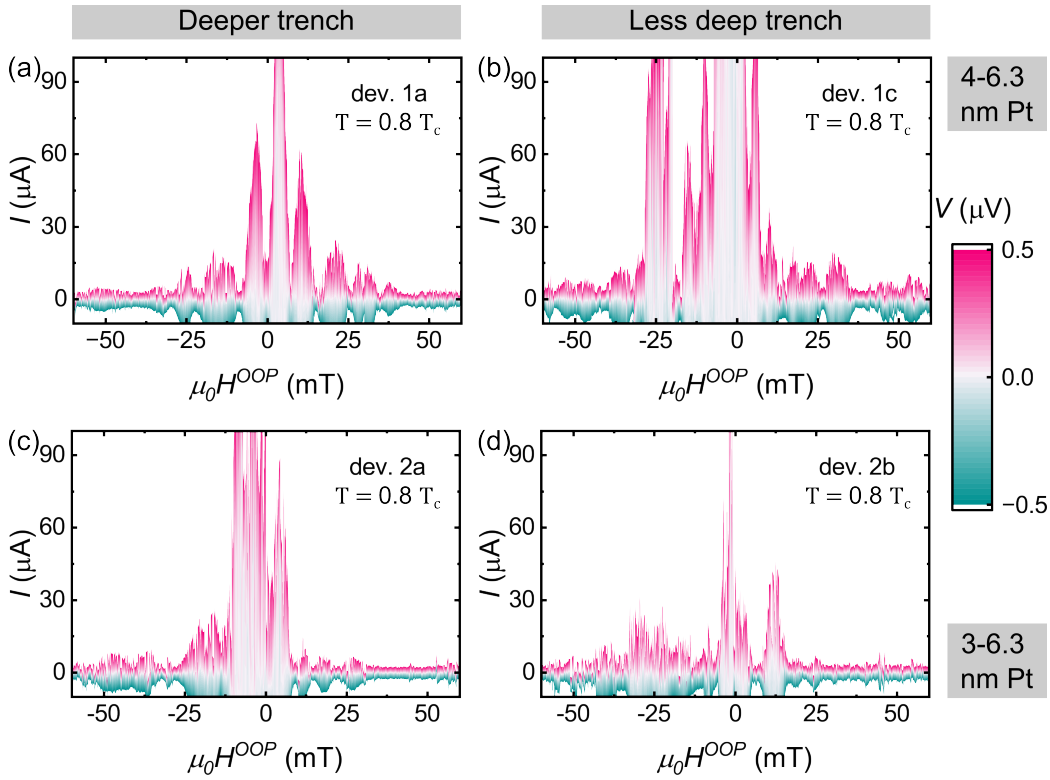

Figure 4.5: *Critical current oscillations with OOP applied magnetic field $\mu_0 H^{OOP}$, measured at $T = 0.8T_c$.* ***Top:*** *devices on sample S1 (4 nm to 6.3 nm Pt),* ***bottom:*** *devices on S2 (3 nm to 6.3 nm Pt).* ***Left:*** *devices with deeper trenches (dev. 1a and 2a),* ***right:*** *devices with less deep trenches (dev. 1c and 2b).*

most reminiscent of a Fraunhofer pattern with oscillation period ~ 8 mT, except the central lobe width is not equal to twice the oscillation period and the second-order lobes are wider than 8 mT. For devices 1c, 2a and 2b, the $I_c(\mu_0 H^{OOP})$ pattern does not have an easily discernible shape, nor do we see a connection between I_c (high or low) and the trench depth (deeper or less deep).

All in all, the $R(T)$ and $I_c(\mu_0 H^{OOP})$ data show that we have junctions in our devices that become fully superconducting. In our lab's experience the S/N/S or S/S′/S junctions that we FIB typically show a Gaussian or Fraunhofer $I_c(\mu_0 H^{OOP})$, so the different $I_c(\mu_0 H^{OOP})$ patterns in Figure 4.5 may indicate that we have indeed the S/N$_{SOC}$/F/N$_{SOC}$/S. In principle, this would directly imply the presence of SOC-generated equal-spin triplets. Nevertheless, the measurements we have discussed so far do not provide sufficient evidence of the nature of the junctions.

4.3 Is the trench 'deep enough'?

The junction devices could potentially provide strong evidence for SOC-mediated LRTC generation but it is essential to know if the trench is cut through the Pt fully, i.e. if the junction is of the type $S/N_{SOC}/F/N_{SOC}/S$. Only then can we indisputably claim an equal-spin triplet supercurrent in a fully superconducting device, since the SRT and singlet would die out in the Co. Hence, the most important remaining question is whether the trench is cut 'deep enough' in any of these devices.

Magnetoresistance

In search of an answer to this question we measure the four-probe normal-state ($T = 10\,\mathrm{K}$) resistance of the devices as a function of the externally applied in-plane magnetic field $\mu_0 H^{IP}$. The field is applied in the direction along the short axis of the bar shape, perpendicular to the zero-field Co magnetization direction that points along the long axis of the bar due to shape anisotropy. Since the current and field directions matter for these measurements, the resistance is now measured as $R = \frac{V(20\mu\mathrm{A}) - V(10\mu\mathrm{A})}{10\mu\mathrm{A}}$ while we sweep the field from 200 mT to −200 mT and back in steps of 1 mT or 2 mT. Due to the anisotropic magnetoresistance (AMR) of the Co, the resistance is expected to reach a maximum when the magnetization is parallel to the current ($\mu_0 H^{IP} = 0$) and decrease as $\mu_0 H^{IP}$ is increased [43]. Differences in magnetoresistance that correlate to trench depth may help determine if the deeper trenches do indeed reach the Co or not.

Figure 4.6 presents the magnetoresistance (MR) measurements for the four devices and we immediately notice an AMR effect in all devices, as a 1.5%-2.1% difference in resistance between $\mu_0 H^{IP} = 0$ and $\mu_0 H^{IP} = 200\,\mathrm{mT}$ (relative to $R(\mu_0 H^{IP} = 200\mathrm{mT})$). Since these measurements are performed at 10 K, the Nb is not superconducting and the current is distributed over the Nb, Pt and Co except at the location of the trench. The AMR ratio is largest in device 1a (2.1%, deeper trench) and smallest in 1c (1.5%, less deep trench), but we do not see the same trend in devices 2a and 2b.

Version of October 13, 2025– Created October 13, 2025 - 11:10

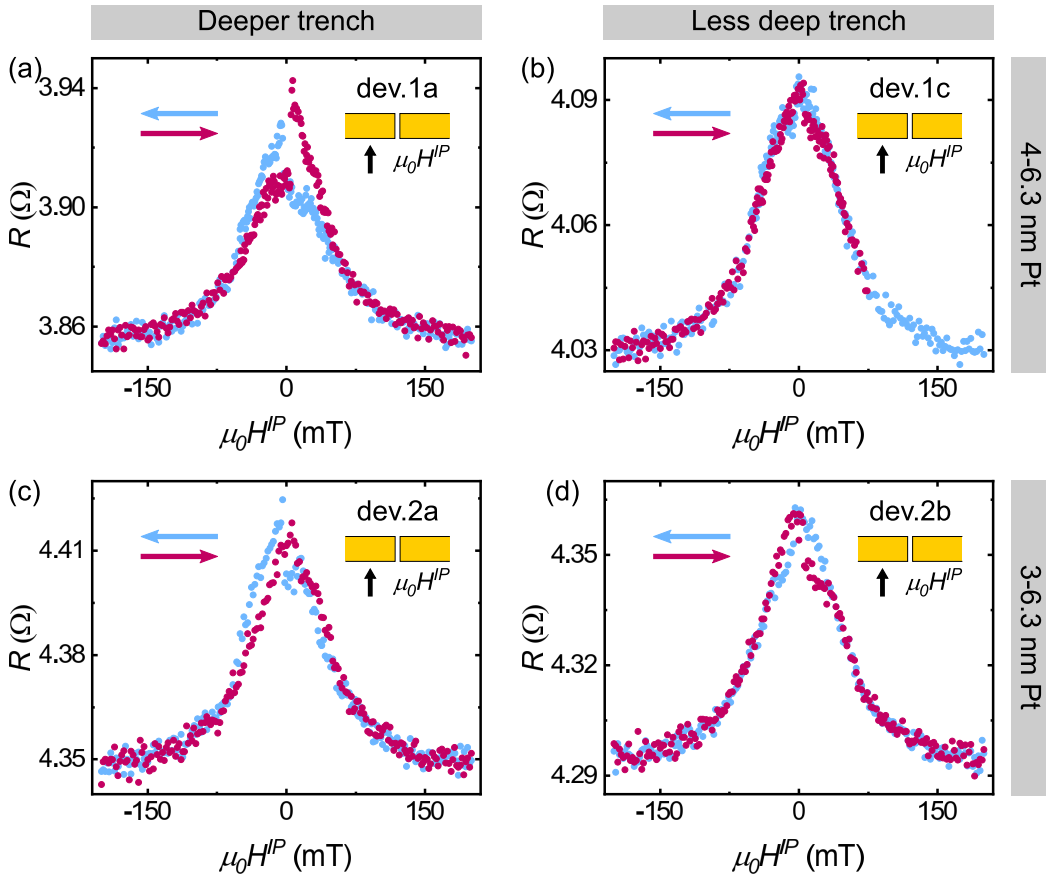

Figure 4.6: *Magnetoresistance measurements with an in-plane external magnetic field perpendicular to the long axis of the bar, as indicated by the insets. The blue data points show the data of the field sweep from* 200 mT *to* −200 mT*, the magenta data points show the data from* −200 mT *to* 200 mT*.* ***Top:*** *devices on sample S1 (*4 nm *to* 6.3 nm *Pt),* ***bottom:*** *devices on S2 (*3 nm *to* 6.3 nm *Pt).* ***Left:*** *devices with deeper trenches (dev. 1a and 2a),* ***right:*** *devices with less deep trenches (dev. 1c and 2b).*

Another notable feature in the MR of device 1a is the jump that occurs near $\mu_0 H^{IP} = 0$. This jump appears when $\mu_0 H^{IP}$ is lowered to zero after magnetizing the Co perpendicular to the current direction: the resistance goes up, but stops at a lower value before jumping up to the original value of the resistance before an external field was applied. A possible explanation is the trapping of a domain with perpendicular magnetization that causes the lower resistance. Curiously, the smaller jumps in the MR measurements of the devices with the less deep trenches (1c and 2b) are jumps *down* to a lower resistance. We currently do not have an explanation for this behavior. Furthermore, the MR of device 2a has no jump at

all; instead, there is displacement of the resistance peak depending on the direction in which the magnetic field was swept, reminiscent of observations in the MR of (unstructured, polycrystalline) Co films [44, 45], and to a smaller extent the same is present in the MR of device 1a.

Although there are some differences between the MR measurements of the four devices, we do not observe structural differences that correlate to the trench depth. Further insight into these measurements requires micromagnetic simulations to see, for instance, what influence the trench has on the formation of magnetic domains in the Co layer. It may well be that the trench has no great influence even if it reaches the Co, since the trench ultimately only occupies 20 nm of the 5 µm length of the bar.

Temperature dependence of the critical current

So far in this work, we have assumed that the trench is 'deep enough' if the trench cuts through the Pt interlayer fully. As a remark on the criterion for the trench to be 'deep enough', it is important to realize that this criterion may differ for LRTC *detection* and *generation*. To be absolutely certain that we have *measured* the LRTC it is necessary to cut the trench all the way through the Pt layer, such that the singlet and short-range triplet components of the condensate certainly die out in the Co. If we know this to be true, then we can be sure there is a LRTC if the device becomes fully superconducting. However, it may not be necessary to cut through the Pt layer fully for the LRTC to be *generated*. A Nb/Pt/Nb junction may already effectively be a $S/F_{SOC}/S$ junction if the Pt is proximity-magnetized[46] by the Co layer.

The possibility of LRTC generation even if the trench does not reach the Co, could provide an explanation for the temperature dependence of the critical current density that is shown in Figure 4.7. These measurements for devices 1a and 1c are obtained with $I(V)$ measurements at different temperatures below and up to just above $T_{c,junction}$ (as determined from Figure 4.4 (c)) from which the critical current I_c is determined. I_c is chosen as the last data point before $V > 1$ µV which, due to the sharp nature of all acquired $I(V)$ data in the Teslatron system, proves to be an accurate measure. In device 1a, we measure critical currents of tens of µA up to 150 µA, while the critical current in device 1c is of the order of hundreds of µA, up to 600 µA.

Version of October 13, 2025– Created October 13, 2025 - 11:10

We estimate the critical current density $J_c = I_c/(w \cdot t)$ based on the width w of the junction (1 µm) and the thickness t as the difference between the total evaporated film thickness and the estimated trench depth. The data is fitted using Equation (4.2), a relation similar to the fit for the upper critical field in Equation (3.4).

$$J_c(T) = J_c(0)(1 - T/T_c)^{\alpha} + J_{c,res} \tag{4.2}$$

Here $J_c(0)$ is the critical current density at $T = 0\,\mathrm{K}$. Due to the finite value of the critical current in all of our data, we could not fit our data using T_c as a fitting parameter. Instead, we used T_c as determined from the Teslatron $R(T)$ measurements in Figure 4.4 (c) where $R = 0$. T_c therefore corresponds to $I_c \leq 10\mu\mathrm{A}$ and this is reflected in the fitting parameter $J_{c,res}$, with which we allowed for a residual critical current density at T_c.

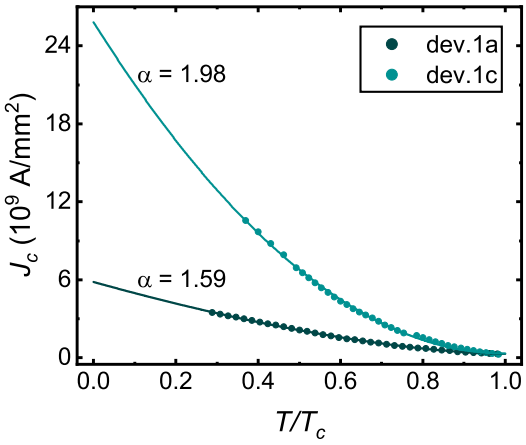

Figure 4.7: *Critical current density as function of the reduced temperature T/T_c for devices 1a (deeper trench) and 1c (less deep trench). Dots indicate experimental data, and solid lines are the fits to Equation (4.2). The power α that results from the fit is annotated near the associated curve, showing an approximately quadratic temperature dependence for device 1c.*

The power α informs us of the possible nature of the supercurrent. In theoretical work on Josephson junctions with a half-metallic ferromagnetic (HMF) weak link, the critical current density for short junctions in the clean limit was found to have a $(1 - T/T_c)^2$ dependence [47, 48]. In such junctions the superconducting transport is carried in full by equal-spin triplets due to the 100% spin-polarization of the HMF. The quadratic dependence was also found experimentally in $La_{0.7}Sr_{0.3}MnO_3$-based junctions where the LRTC is generated [9]. Meanwhile, the expected tempera-

Version of October 13, 2025– Created October 13, 2025 - 11:10

ture dependence of J_c for short junctions with a normal metal weak link is $(1 - T/T_c)$ [49].

Our results in Figure 4.7 show a near-quadratic dependence for device 1c (less deep trench) with $\alpha = 1.98 \pm 0.02$. In the device with the deeper trench (1a), the T-dependence fits to $\alpha = 1.59 \pm 0.01$. If $\alpha = 1.98$ is indicative of the LRTC in device 1c, then the deeper trench in device 1a can intuitively explain the lower value for α. We assume it would then be likely that the trench in device 1a is deep enough to cut into the Co, making the junction longer and further removed from the Nb/Pt interface. However, the theory that Eschrig and Löfwander [47] developed may not be directly applicable to our devices since Co is not a HMF.

Then let us *not* assume the presence equal-spin triplets. Our junctions are still in the short junction limit, regardless of the depth of the trench: $\xi_{Nb} \approx 10\,\text{nm}$ to $15\,\text{nm}$ and we estimate $\xi_{Pt} \approx 10\,\text{nm}$ based on the scanning tunneling spectroscopy measurement of 10 nm Pt on Nb by Flokstra *et al.* [18]. Both are of the same order magnitude as the junction length, which is $\sim$20 nm. Furthermore, the junction length only starts to increase if we cut into the Co, but to have any superconducting transport in that case *requires* the LRTC by default. Thus, if we do not assume the LRTC, we can assume a short junction. For a short junction, our finding that $J_c \propto (1 - T/T_c)^{1.98}$ is heavily anomalous in light of the expected $\propto (1 - T/T_c)$ dependence.

Version of October 13, 2025– Created October 13, 2025 - 11:10

Chapter 5

Conclusions

In summary, we have performed transport measurements on Au/Nb/Pt/Co, Au/Nb/Pt and Au/Nb/Co samples for evidence of Rashba SOC-mediated generation of equal-spin triplets in Nb/Pt/Co. Our samples include films that are structured with EBL into 20 µm×20 µm squares for a Van der Pauw configuration, and 1 µm×5 µm bar-shaped devices with Josephson junctions structured with FIB.

One striking result is the low T_c of the Au/Nb/Pt/Co film, which is 2 K lower than the T_c of the films with Pt *or* Co. With only 15 nm Nb, superconductivity in these films is suppressed by proximity and pair-breaking effects, resulting in reduced T_c. In addition, upper critical field measurements reveal that the superconducting condensate is least 2D-like in the Au/Nb/Pt/Co film and its coherence length is 50% larger than for Au/Nb/Pt and Au/Nb/Co. These observations can be consistent with enhanced proximity in Co due to LRTC generation, but other explanations, such as increased interface transparency, are possible. We must also note that the geometry of these samples resembles the transversal geometry with in-plane magnetization that according to Bergeret and Tokatly [15] cannot produce the LRTC with only Rashba SOC. A lateral geometry is preferred.

Our devices feature lateral Nb/Pt/Co/Pt/Nb junctions that could potentially provide irrefutable evidence for SOC-mediated LRTC generation. $R(T)$ measurements show that the devices become fully superconducting and their $I_c(\mu_0 H^{OOP})$ patterns confirm junctions. We find that a deeper FIB trench and a thinner Pt layer are both related to a lower junction T_c. These results are all consistent with the LRTC, but they are also perfectly in agreement with regular singlet superconductivity if we lack proof that

Version of October 13, 2025– Created October 13, 2025 - 11:10

the FIB trench is deep enough to create a Nb/Pt/Co/Pt/Nb junction.

Finally, the temperature dependence of the critical current density of our junction devices is anomalous if we do not assume the LRTC. We find $J_c(T) \propto (1 - T/T_c)^{1.98}$ for a device with a less deep trench, and $J_c \propto (1 - T/T_c)^{1.59}$ for a deeper trench, whereas $\propto (1 - T/T_c)$ is expected in the short junction limit if we have a Nb/Pt/Nb or constriction junction. A quadratic temperature dependence may indicate equal-spin triplet transport according to Eschrig and Löfwander [47], although their theory was developed for HMFs and therefore may not be directly applicable to our samples.

The main limitation on the conclusions that we can draw from our measurements is that we do not know the accuracy of the trench depth estimates. It is possible that the cross-sectional line measurement method provides an overestimation, in which case it may well be that none of the devices has a Nb/Pt/Co/Pt/Nb junction. Magnetoresistance measurements of the devices do not offer sufficient insight into the matter. Alternatively, performing a cleaning cut cross-section with FIB might be a better option to estimate the trench depth. The biggest difficulty is that over-milling is also not desired: if the trench is *too* deep, the junction will become too long even for the LRTC to survive. This introduces the complication that, if the trench certainly cuts into the Co, a non-superconducting device could indicate either the absence of the LRTC or a too deep trench. Thus, the trench depth is a highly delicate parameter in these devices that we do not have adequate control over at present.

Further efforts should therefore first focus on films to investigate the nature of the lower T_c and larger $\xi(0)$ in the Au/Nb/Pt/Co sample, where it could be fruitful to vary the thickness of the Pt layer or produce trilayers (such as Co/Pt/Nb/Pt/Co) to improve the symmetry of the samples. The more involved junction devices could be studied by producing many with varying trench depths and perhaps this would shine light on the trench depth issue.

We have not unequivocally confirmed the SOC-mediated LRTC in this work, nor have we completely refuted it. However, our measurements of the films and $J_c(T)$ of the junction devices do harbor some surprises that provide grounds for further fundamentally interesting research into Pt and the SOC-generated LRTC.

Version of October 13, 2025– Created October 13, 2025 - 11:10

Acknowledgments

I am grateful to Prof. dr. Jan Aarts for the opportunity to conduct this research under his guidance. Our meetings have always reignited my curiosity and renewed my energy, and Jan has been very involved and interested as a supervisor. Possessing decades of knowledge and experience, he has given much advice, but also encouraged me to be an independent researcher.

Furthermore, I would like to thank Julian van Doorn for helping me get started in the first stages of this project, and for the FIB milling of the samples. I also thank Tycho Blom for his FIB milling services, although those samples unfortunately did not make it into this thesis.

Finally, I extend my gratitude to Luc Wigbout for our fruitful discussions and, in general, his everlasting love and support.

References

[1] Igor Žutić. "Spintronics: Fundamentals and applications." In: *Reviews of Modern Physics* 76.2 (2004). DOI: 10.1103/RevModPhys.76.323.

[2] Jacob Linder and Jason W. A. Robinson. "Superconducting spintronics." In: *Nature Physics* 11.4 (2015). DOI: 10.1038/nphys3242.

[3] M. Houzet and A. I. Buzdin. "Long range triplet Josephson effect through a ferromagnetic trilayer." In: *Physical Review B* 76.6 (2007). DOI: 10.1103/PhysRevB.76.060504.

[4] J. W. A. Robinson, J. D. S. Witt, and M. G. Blamire. "Controlled Injection of Spin-Triplet Supercurrents into a Strong Ferromagnet." In: *Science* 329.5987 (2010). DOI: 10.1126/science.1189246.

[5] Carolin Klose *et al.* "Optimization of Spin-Triplet Supercurrent in Ferromagnetic Josephson Junctions." In: *Physical Review Letters* 108.12 (2012). DOI: 10.1103/PhysRevLett.108.127002.

[6] Remko Fermin *et al.* "Superconducting Triplet Rim Currents in a Spin-Textured Ferromagnetic Disk." In: *Nano Letters* 22.6 (2022). DOI: 10.1021/acs.nanolett.1c04051.

[7] R. S. Keizer *et al.* "A spin triplet supercurrent through the half-metallic ferromagnet CrO2." In: *Nature* 439.7078 (2006). DOI: 10.1038/nature04499.

[8] M. S. Anwar *et al.* "Long-range supercurrents through half-metallic ferromagnetic CrO_2." In: *Physical Review B* 82.10 (2010). DOI: 10.1103/PhysRevB.82.100501.

[9] Yao Junxiang *et al.* "Triplet supercurrents in lateral Josephson junctions with a half-metallic ferromagnet." In: *Physical Review Research* 6.4 (2024). DOI: 10.1103/PhysRevResearch.6.043114.

[10] Nathan Satchell and Norman O. Birge. "Supercurrent in ferromagnetic Josephson junctions with heavy metal interlayers." In: *Physical Review B* 97.21 (2018). DOI: 10.1103/PhysRevB.97.214509.

[11] N. Banerjee *et al.* "Controlling the superconducting transition by spin-orbit coupling." In: *Physical Review B* 97.18 (2018). DOI: 10.1103/PhysRevB.97.184521.

[12] Kun-Rok Jeon *et al.* "Enhanced spin pumping into superconductors provides evidence for superconducting pure spin currents." In: *Nature Materials* 17.6 (2018). DOI: 10.1038/s41563-018-0058-9.

[13] Kun-Rok Jeon *et al.* "Exchange-field enhancement of superconducting spin pumping." In: *Physical Review B* 99.2 (2019). DOI: 10.1103/PhysRevB.99.024507.

[14] Kun-Rok Jeon *et al.* "Tunable Pure Spin Supercurrents and the Demonstration of Their Gateability in a Spin-Wave Device." In: *Physical Review X* 10.3 (2020). DOI: 10.1103/PhysRevX.10.031020.

[15] F. S. Bergeret and I. V. Tokatly. "Spin-orbit coupling as a source of long-range triplet proximity effect in superconductor-ferromagnet hybrid structures." In: *Physical Review B* 89.13 (2014). DOI: 10.1103/PhysRevB.89.134517.

[16] F. S. Bergeret and I. V. Tokatly. "Singlet-Triplet Conversion and the Long-Range Proximity Effect in Superconductor-Ferromagnet Structures with Generic Spin Dependent Fields." In: *Physical Review Letters* 110.11 (2013). DOI: 10.1103/PhysRevLett.110.117003.

[17] Nathan Satchell, Reza Loloee, and Norman O. Birge. "Supercurrent in ferromagnetic Josephson junctions with heavy-metal interlayers. II. Canted magnetization." In: *Physical Review B* 99.17 (2019). DOI: 10.1103/PhysRevB.99.174519.

[18] Machiel Flokstra *et al.* "Spin-orbit driven superconducting proximity effects in Pt/Nb thin films." In: *Nature Communications* 14.1 (2023). DOI: 10.1038/s41467-023-40757-1.

[19] Anderson Paschoa *et al.* "Colossal superconducting spin-valve effect in superconductor-non-magnetic metal heterostructure mediated by spin-orbit coupling." In: *Applied Physics Letters* 124.22 (2024). DOI: 10.1063/5.0202337.

[20] Kelsey B. Robbins *et al.* "Upper critical fields in normal metal–superconductor–normal metal trilayers." In: *Scientific Reports* 15.1 (2025). DOI: 10.1038/s41598-025-98332-1.

[21] K. Lahabi. "Spin-triplet supercurrents of odd and even parity in nanostructured devices." PhD thesis. Leiden University, 2018.

[22] Nicola Pinto *et al.* "Dimensional crossover and incipient quantum size effects in superconducting niobium nanofilms." In: *Scientific Reports* 8.1 (2018). DOI: 10.1038/s41598-018-22983-6.

[23] Sameh M. Altanany *et al.* "Vortex dynamics in disordered niobium thin films." In: *Physical Review B* 109.21 (2024). DOI: 10.1103/PhysRevB.109.214504.

[24] Matthias Eschrig. "Spin-polarized supercurrents for spintronics: a review of current progress." In: *Reports on Progress in Physics* 78.10 (2015). DOI: 10.1088/0034-4885/78/10/104501.

[25] A. Manchon *et al.* "New perspectives for Rashba spin-orbit coupling." In: *Nature Materials* 14.9 (2015). DOI: 10.1038/nmat4360.

[26] G. Bihlmayer, O. Rader, and R. Winkler. "Focus on the Rashba effect." In: *New Journal of Physics* 17.5 (2015). DOI: 10.1088/1367-2630/17/5/050202.

[27] Dario Bercioux and Procolo Lucignano. "Quantum transport in Rashba spin-orbit materials: a review." In: *Reports on Progress in Physics* 78.10 (2015). DOI: 10.1088/0034-4885/78/10/106001.

[28] Gustav Bihlmayer *et al.* "Rashba-like physics in condensed matter." In: *Nature Reviews Physics* 4.10 (2022). DOI: 10.1038/s42254-022-00490-y.

[29] Yu. A. Bychkov and É. I. Rashba. "Properties of a 2D electron gas with lifted spectral degeneracy." In: *Soviet Journal of Experimental and Theoretical Physics Letters* 39 (1984).

[30] Lev P. Gor'kov and Emmanuel I. Rashba. "Superconducting 2D System with Lifted Spin Degeneracy: Mixed Singlet-Triplet State." In: *Physical Review Letters* 87.3 (2001). DOI: 10.1103/PhysRevLett.87.037004.

[31] Morten Amundsen *et al.* "Colloquium: Spin-orbit effects in superconducting hybrid structures." In: *Reviews of Modern Physics* 96.2 (2024). DOI: 10.1103/RevModPhys.96.021003.

[32] Yangkun He *et al.* "Au_4Mn: A localized ferromagnet with strong spin-orbit coupling, long-range ferromagnetic exchange, and high Curie temperature." In: *Physical Review B* 106.21 (2022). DOI: 10.1103/PhysRevB.106.214414.

[33] Emilio Vélez-Fort *et al.* "Ferromagnetism and Rashba Spin-Orbit Coupling in the Two-Dimensional (V,Pt)Se2 Alloy." In: *ACS Applied Electronic Materials* 4.1 (2022). DOI: 10.1021/acsaelm.1c00992.

[34] P. Koorevaar, R. Coehoorn, and J. Aarts. "Critical fields in vanadium-based superconducting/ferromagnetic multilayers." In: *Physica C: Superconductivity* 248.1 (1995). DOI: 10.1016/0921-4534(95)00235-9.

[35] Chen Pang and Yi Zhou. "Interplay of Zeeman field, Rashba spin-orbit interaction, and superconductivity: Transition temperature and quasiparticle excitations." In: *Science China Physics, Mechanics & Astronomy* 68.7 (2025). DOI: 10.1007/s11433-024-2658-6.

[36] Shunsuke Yoshizawa *et al.* "Atomic-layer Rashba-type superconductor protected by dynamic spin-momentum locking." In: *Nature Communications* 12.1 (2021). DOI: 10.1038/s41467-021-21642-1.

[37] J. Aarts *et al.* "Interface transparency of superconductor/ferromagnetic multilayers." In: *Physical Review B* 56.5 (1997). DOI: 10.1103/PhysRevB.56.2779.

[38] Michael Tinkham. *Introduction to Superconductivity*. 2nd ed. Mineola, NY: Dover Publications, Inc., 2004. ISBN: 978-0-486-43503-9.

[39] Marianna Magni, Diego Scaccabarozzi, and Bortolino Saggin. "Compensation of Thermal Gradients Effects on a Quartz Crystal Microbalance." In: *Sensors* 23.1 (2023). DOI: 10.3390/s23010024.

[40] Ning Li *et al.* "Effect of quartz crystal thermal stress on its performance in active temperature control quartz crystal microbalance dew point sensors." In: *Sensors and Actuators B: Chemical* 369 (2022). DOI: 10.1016/j.snb.2022.132283.

[41] Günter Sauerbrey. "Verwendung von Schwingquarzen zur Wägung dünner Schichten und zur Mikrowägung." In: *Zeitschrift fur Physik* 155 (1959). DOI: 10.1007/BF01337937.

[42] *QCM100 - Quartz Crystal Microbalance Theory and Calibration*. 2019.

[43] M. El-Tahawy *et al.* "Anisotropic magnetoresistance (AMR) of cobalt: hcp-Co vs. fcc-Co." In: *Journal of Magnetism and Magnetic Materials* 560 (2022). DOI: 10.1016/j.jmmm.2022.169660.

[44] M. Viret *et al.* "Spin scattering in ferromagnetic thin films." In: *Physical Review B* 53.13 (1996). DOI: 10.1103/PhysRevB.53.8464.

[45] Woosik Gil. "Magnetoresistance anisotropy of polycrystalline cobalt films: Geometrical-size and domain effects." In: *Physical Review B* 72.13 (2005). DOI: 10.1103/PhysRevB.72.134401.

[46] Kun-Rok Jeon *et al.* "Zero-field polarity-reversible Josephson supercurrent diodes enabled by a proximity-magnetized Pt barrier." In: *Nature Materials* 21.9 (2022). DOI: 10.1038/s41563-022-01300-7.

[47] Matthias Eschrig and Tomas Löfwander. "Triplet supercurrents in clean and disordered half-metallic ferromagnets." In: *Nature Physics* 4.2 (2008). DOI: 10.1038/nphys831.

[48] M. Eschrig. "Theory of Half-Metal/Superconductor Heterostructures." In: *Physical Review Letters* 90.13 (2003). DOI: 10.1103/PhysRevLett.90.137003.

[49] K. K. Likharev. "Superconducting weak links." In: *Reviews of Modern Physics* 51.1 (1979). DOI: 10.1103/RevModPhys.51.101.